Synaptic and mitochondrial plasticity associated with fear memory revealed by deep learning-based 3D reconstruction

Jing Liu[1,2#], Junqian Qi[3#], Xi Chen[1#], Zhenchen Li[2#], Bei Hong[1,2], Hongtu Ma[1], Guoqing Li[1], Lijun Shen[1], Danqian Liu[4], Yu Kong[4], Qiwei Xie[5*], Hua Han[1,2,4*], and Yang Yang[3*]

1. Research Center for Brain-inspired Intelligence, Institute of Automation, Chinese Academy of Sciences, Beijing, China
2. School of Artificial Intelligence, School of Future Technology, University of Chinese Academy of Sciences, Beijing, China
3. School of Life Science and Technology, ShanghaiTech University, Shanghai, China
4. Institute of Neuroscience, Center for Excellence in Brain Science and Intelligence Technology, Chinese Academy of Sciences, Shanghai, China
5. Research Base of Beijing Modern Manufacturing Development, Beijing University of Technology, Beijing, China

#These authors contributed equally to this work

*To whom the correspondence should be addressed (E-mail: qiwei.xie@bjut.edu.cn, hua.han@ia.ac.cn, yangyang2@shanghaitech.edu.cn)

Abstract

Reconstruction of serial section electron microscopy (ssEM) data greatly facilitates neuroscience research, but such reconstruction is computationally expensive. Informative data about physiological functions can in theory be obtained from ssEM datasets by extracting distinct cellular structures without large-scale reconstruction, but an efficient method is needed to accomplish this. Here, we developed a Region-CNN (R-CNN) based deep learning method to identify, segment, and reconstruct synapses and mitochondria from ssEM data. We applied this method to explore the changes in synaptic and mitochondrial configuration in the auditory cortex of mice subjected to auditory fear conditioning. Upon reconstructing over 135,000 mitochondria and 160,000 synapses, we found that fear conditioning significantly increases the number—while decreasing the size—of mitochondria, and also noted that it promoted the formation of multi-contact synapses comprising a single axonal bouton and multiple postsynaptic sites from different dendrites. Combinatorial modeling indicated that such multi-dendritic synapses increased information storage capacity of new synapses by over 50%, representing a synaptic memory engram. Our method achieved high accuracy and speed in synapse and mitochondrion extraction, and its application revealed structural and functional insights about cellular engrams associated with fear conditioning.

Introduction

The mammalian brain consists of a vast and complex network of neurons interconnected by specialized sites called synapses. In this network, a neuron may receive input from, and send output to, thousands of other neurons. The concerted activities of neurons, which encode, process, and store information, fundamentally depend on the connectivity patterns of synapses. Thus, it is critical to elucidate the organization of synaptic circuits in order to understand brain functions.

Dissecting the synaptic circuit is technically challenging due to small size, complex morphology, dense distribution, and enormous number of synapses. Light microscopy has been used to examine populations of synapses *in vitro* and *in vivo*. Previous work has shown that learning effectively modifies synaptic structures of the mammalian cerebral cortex[1-3]. Auditory fear conditioning (AFC), a common paradigm of associative learning, increases formation of presynaptic boutons and postsynaptic spines in the auditory cortex (A1)[3]. However, although boutons and spines can be visualized using light microscopy, the width of the synaptic cleft is below the diffraction limit and therefore synapses are difficult to discern using light microscopy images[4]. The serial-section electron microscopy (ssEM) technique[5] overcomes the resolution problem and enables large-scale three-dimensional (3D) reconstruction of brain tissue with nanometer-scale resolution, which is sufficient to resolve the ultrastructural features of synapses, such as presynaptic vesicles, the synaptic cleft, and the

postsynaptic density (PSD). However, manual identification and segmentation of synapses from massive ssEM datasets is extremely time-consuming, and thus requires an automated pipeline.

To date, a variety of machine learning-based approaches for synapse detection have been proposed. Some methods require saturated reconstruction or segmentation of neuronal structures prior to synapse detection[6, 7], which themselves are daunting tasks for large datasets. Other methods do not make full use of the contextual information or structural properties of synapses[8, 9], making them more prone to errors. Some other methods require nearly isotropic imaging data[10], a requirement incompatible with standard ssEM, in which the axial resolution (section thickness) is typically much worse than the lateral resolution. Most recently, an indirect method detect synapses by identify the synaptic connectivity (pre- and postsynaptic component of each synapse)[11]. Therefore, there is much to be desired in terms of the identification accuracy, speed, and general applicability of automated synapse analysis tools.

Mitochondria have essential roles in cellular functions, such as producing adenosine triphosphate (ATP) and calcium homeostasis[12]. Moreover, synaptic mitochondria are linked to the process of neurotransmitter release and organization of synaptic vesicles[13]. In the past decade, ssEM has been increasingly used to investigate mitochondrial structures. Along with this, a variety of automated methods have been developed to detect mitochondria from ssEM images. One method is based on handcrafted features and traditional classifiers[14-16], the other is based on powerful 2D or 3D convolutional neural networks (CNNs)[10, 17].

In this study, we used Region-CNN (R-CNN) based deep learning algorithms to identify, segment, and reconstruct synapses and mitochondria from ssEM images of the mouse auditory cortex. Our pipeline achieved state-of-the-art accuracy with a speed two orders of magnitude faster than human experts, enabling us to sample more than one hundred thousand synapses and mitochondria. Using this method, we studied how a classical learning model, namely AFC, affects the synaptic and mitochondrial organization in the A1 (Figure 1). Using large-scale synapse reconstruction together with mathematical modeling, we found that AFC increases multi-synaptic boutons connecting one axonal bouton to multiple different dendrites in the A1, and these 1-to-N connections dramatically increased the information coding capacity, thus representing a synaptic memory engram.

Results

Auditory fear conditioning as a model for learning and memory

To investigate changes in cellular structures induced by learning and memory in the adult brain, we used a simple and robust behavioral model for associative learning:

auditory fear conditioning (AFC). Specifically, conditioned mice received 5 sessions of paired tone pips (conditioned stimulus, CS) and foot shock (unconditioned stimulus, US), while control mice received 5 sessions of just tone pips (Figure 1A). Mice were tested with the conditioned stimulus 24 hours after conditioning. All conditioned mice (n = 3) exhibited a high freezing response, while all control mice (n = 3) exhibited a low freezing response as expected (Extended Data Figure 1). At 4 days after conditioning, we harvested auditory cortex (A1) tissue blocks from these mice and prepared them for ssEM (Figure 1A). We sectioned and imaged a total of 2.8×10^5 μm^3 A1 tissue at 2-4 nm lateral resolution and 50 nm section thickness for ssEM imaging and reconstruction.

Deep learning-based reconstruction of synapses in A1

We first explored synaptic changes associated with AFC, by extracting structural information of synapses from ssEM data. Synapses have distinct ultrastructural properties: pre- and postsynaptic membranes with a synaptic cleft in between, postsynaptic density (PSD) and abundant synaptic vesicles in presynaptic terminals. These special features enabled us to design a 2D-3D pipeline to detect and reconstruct synapses at the two-dimensional (2D) and 3D levels. Due to the high anisotropy of voxels (x-y resolution: 2-4 nm, z: 50 nm) and intrinsic local misalignments in most ssEM data, using a 3D convolutional neural network (3D CNN) increases the computational complexity without offering any improvement in performance.

At the 2D level, we used the Mask R-CNN[18] model to detect and segment synapses in each 2D image (Figure 2A). The Mask R-CNN is a deep neural network for instance segmentation, which can separate distinct objects in an image. As illustrated in Figure 2B, Mask R-CNN is composed of three primary parts: backbone network, Region Proposal Network (RPN) and Region-CNN (R-CNN). The backbone network provides shared feature maps for the other two parts. The backbone used for synapse detection is a Feature Pyramid Network (FPN, Methods, Figure 2B)[19], which we modified from the ResNet50 model[20]. As a typical two-stage detector, it first generates enough region proposals to guarantee the pre-specified recall rate with a RPN. Subsequently, the feature maps of the proposals are extracted as Regions of Interest (RoIs). R-CNN then makes further classification (predicting the scores being synapses or not), regression (predicting the coordinates of synapses' bounding boxes) and predicts a pixel level mask for the RoIs identified in the first stage. The classification branch that predicted each RoI as a synaptic or non-synaptic object explored both the features of the synaptic vesicles and the PSD. This second stage guarantees the precision rate. After obtaining the final positions, the mask branch predicted the segmentation masks of the detected PSDs.

To train the network, a total of 600 ssEM images from the aforementioned A1 dataset were annotated by two expert annotators with cross-validation (two volumes of 2,048 × 2,048 × 300 voxels for the control and conditioned groups, respectively),

which was split into training (60%), validation (20%), or test (20%) sets. Evaluation against the test set showed that our pipeline achieved a 0.90 precision rate and a 0.83 recall rate for synapse detection (Extended Data Figure 4A and 4C).

To quantitatively evaluate the performance (efficiency and accuracy) of the Mask R-CNN, we compared it against other state-of-the-art CNNs using a previously reported public ssEM dataset[1] comprising 178 slices sized 8576×7616 pixels. The dataset is divided into two equal parts, one for training and one for testing. The baseline network U-Net[21] and the 3D U-Net[22] are commonly used for biomedical image segmentation tasks. In terms of precision rate, recall rate, and F1-score (the harmonic mean of precision and recall), our pipeline outperformed U-Net and 3D U-Net (Figure 2E).

We also compared the running time of the three networks equipped with one graphics processing unit (GPU) as well as the time consumption of complete manual annotation (Figure 2F). The results confirmed that the speed of our method ($1.27 \times 10^{11} \pm 1.44 \times 10^{10}$ voxels/day) is in the same order of magnitude as 3D U-Net ($1.40 \times 10^{11} \pm 1.39 \times 10^{10}$ voxels/day), one order of magnitude faster than U-Net ($7.33 \times 10^{10} \pm 8.40 \times 10^{9}$ voxels/day), but two orders of magnitude faster than that manual annotation (1.77×10^{8} voxels/day).

At the 3D level, we used a 3D connection algorithm (Figure 2C) to find the instance-level connected components and reconstruct synapses. Based on the continuity of the aligned ssEM volume and the spatial structure of the synapses, we constructed similarity matrices (Methods) between adjacent layers with synapse detection boxes. If the similarity of the two bounding boxes was greater than a certain threshold (0.5), we considered the corresponding synapse to be the same one at the 3D level. If a synapse appeared in more than 3 continuous layers, it was retained and given a unique label; otherwise, it was discarded as a false positive. Therefore, this connection algorithm was also used as a post-processing method to remove false positives and refine the segmentation and detection results. After connected component labeling, we could obtain the synaptic instance segmentation results where each label indicated a unique synapse in 3D.

Using our 2D-3D pipeline, we automatically extracted ultrastructural information of all synapses (Extended Data Figure 3), including synapses formed on dendritic spines and shafts, from the mouse A1 tissue blocks. We identified, segmented, and reconstructed over 160,000 synapses from 12 image stacks of 6 mice. To compare the spatial distribution of synapses in control and conditioned animals, we computed the distance between any two synapses, and found that synapses were uniformly distributed both in control and conditioned animals (Figure 2D). Therefore, AFC does not cause a major change in synapse number and distribution in A1.

[1] https://www.micro-visions.org/data/Synapse-ATUM/

Deep learning-based reconstruction of mitochondria in A1

We designed our 2D-3D pipeline such that it is capable of identifying any cellular compartment or organelle with borders and distinct structural properties. We thus also used our pipeline to identify mitochondria, the major energy source for cellular functions and neuronal activities, from the same ssEM dataset. Mask R-CNN first predicted a binary mitochondrial mask (Figure 3A) of each input image, after which the 3D connection algorithm produced the reconstructed mitochondria (Figure 3B). To build a groundtruth mitochondria dataset, mitochondria from 20 images (7,492 × 7,492 pixels) were labeled by experienced annotators. The train-validation-test split ratio used here was same as for synapses. To correct for discrepancies in imaging conditions, we preprocessed the images using histogram matching. The images were cropped into smaller patches (1,024 × 1,024 pixels) for training the R-CNN. The proposed algorithm achieved a 0.96 precision rate and a 0.81 recall rate for mitochondria on the test set.

After validation against the groundtruth dataset, we applied the 2D-3D pipeline to study changes in mitochondrial configuration after fear conditioning. We identified, segmented, and reconstructed over 135,000 mitochondria from 12 image stacks of 6 mice in A1. By combining the synapse dataset and mitochondria dataset, we found PSD areas of presynaptic bouton with mitochondria were larger than those without mitochondria (synapse with mitochondria: 0.21 ± 0.008 μm^2, synapse without mitochondria: 0.12 ± 0.002 μm^2, Figure 3F). Surprisingly, fear conditioning significantly decreased mitochondrial volumes (control: 0.11 ± 0.003 μm^3, conditioned: 0.08 ± 0.001 μm^3, Figure 3D), however, increased mitochondrial density (control: 0.57 ± 0.023 μm^3, conditioned: 0.65 ± 0.014 μm^3, Figure 3E). Thus although AFC does not alter the spatial distribution of synapses, it increases the number while decreases the size of mitochondria.

A synapse dataset combined with mitochondria and synaptic vesicles

We successfully quantified the number and size of mitochondria and PSD of synapses from ssEM images in A1 with our 2D-3D pipeline, but the pre- and postsynaptic sites of each synapse (*i.e.*, synaptic connectivity) are still unclear. Vesicle cloud in the presynaptic terminal provides essential information for distinguishing axon or dendrite segments in ssEM images, i.e., presynaptic and postsynaptic neurons of each synapse. The 2D level vesicle segmentation is sufficient without the need to produce detection results. Thus, we applied FusionNet[23], a variant of U-Net, to detect the synaptic vesicle clouds (Extended Data Figure 5A). FusionNet used the residual blocks and summation-based skip connections (Extended Data Figure 5B), which could achieve state-of-the-art performance in the segmentation task of the ssEM data. The network output probability maps each element indicating the probability of belonging to the foreground. Synaptic vesicles were about 60 nm in diameter and concentrated in the presynaptic

region. Since labeling them individually would be extremely time-consuming, we annotated vesicle clouds to reduce the annotation workload. We extracted two volumes (2,048 × 2,048 × 50 voxels) for synaptic vesicle annotation, and divided them into training, validation, and test sets using the same split ratio as for synapses and mitochondria. To evaluate the performance on the test set, a thresholding operation was conducted, and FusionNet yielded a precision rate of 0.83 and a recall rate of 0.80.

After applying the trained version of FusionNet to identify vesicle clouds in A1, we constructed a large-scale dataset containing synapses, mitochondria and vesicles from control and conditioned mice, which can be used then for studying the cellular ultrastructural changes associated with AFC. An example showing synaptic ultrastructure, including synaptic cleft, mitochondria, and vesicle cloud, is presented in Figure 3G.

Fear conditioning increased a specific type of multi-contact synapses

Synapses that form 1-to-N or N-to-1 connections, termed multiple-contact synapses (MCSs), have been observed in the brains of mice, rabbits and monkeys[24-26], and were implicated in special functions such as memory storage associated with eye-blink conditioning [27]. But statistical and structural analyses were limited due to the small sample size obtained by manual notation of EM data in previous studies. In our previous work, we found that in A1, synaptogenesis rarely occurs *de novo*, but rather by addition of new boutons or spines to existing counterparts. The finding that AFC leads to an increase in spine and bouton formation together with the "partial addition rule" may lead to an increase in MCSs, if the additions are not accompanied by eliminations of existing synapses *via* synaptic competition.

To find out if MCSs serve as a synaptic memory engram for AFC, we designed a semi-automated method to localize all MCSs in the tissue blocks, in order to study MCSs in a large scale (Figure 4A and Extended Data Figure 8A). As the MCSs contain the same bouton or the same spine, the distances of multiple postsynaptic or presynaptic sites are restricted in a certain scope (~ 1- μm). Based on this biological prior information, the candidate MCSs were detected by restricting the distances between identified synapses. Then expert annotators proofread to exclude the false positives (Figure 4B) which were not easily distinguished in 2D images. By combining the segmentation results of synapses and vesicle clouds to estimate the number of boutons in one MCS, we then classified all the identified MCSs into two types: those consisting of a single bouton contacting multiple postsynaptic sites ("Multi-Synaptic Bouton", MSB, Figure 4C and 4D) or those consisting of a single spine contacting multiple boutons ("Multi-Synaptic Spine", MSS, Figure 4E).

We found that the percentage of MSB synapses was significantly increased after fear conditioning (control: 5.0 ± 0.3 %, conditioned: 6.8 ± 0.2 %, Figure 4F), whereas that of MSS synapses did not change (control: 1.8 ± 0.4 %, conditioned: 1.4 ± 0.4 %, Figure

4G). We also noted that the majority (~98.58 ± 0.4%) of MSBs had 2 postsynaptic targets, yet a few had 3 or more (Figure 4D), and the percentage of MSBs forming more than 2 synapses was significantly elevated higher in the conditioned animals (control: 1.07 ± 0.3%, conditioned: 2.26 ± 0.3 %, Extended Data Figure 8D). Together, these results showed that fear conditioning affects MCSs, specifically by promoting formation of MSBs. We also found that the percentage of MSB synapses with presynaptic mitochondria is significantly higher than the percentage of single-synaptic bouton (SSB) synapses with presynaptic mitochondria (MSB: 59.41 ± 1.3%, SSB: 34.12 ± 0.6%, Figure 4H), indicating that MSBs are more energy-demanding.

Combinatorial modeling to assess bouton and spine turnover patterns

Synapses undergo constant turnover in the adult brain, and long-term memory storage may involve the formation of new synapses[1-3]. However, it is unclear to what extent such synaptic additions may be accompanied by the elimination of existing synapses (or whether they tend to co-exist). We addressed this question using our MSS/MSB dataset combined with *in vivo* imaging results. We performed *in vivo* two-photon imaging of fluorescently labeled boutons and spines in A1 of control and fear conditioned mice, and computed the bouton and spine turnover rates at 4 days after AFC. The formation and elimination rates of spines over the 4-day period are 9.7 ± 1.02% and 8.9 ± 0.41%, and of boutons 14.7 ± 1.03% and 17.8 ± 1.24%, with no significant net increase or decrease. We reasoned that if the addition of a new synaptic bouton/spine is always accompanied by the elimination of an existing bouton/spine (Figure 5A), then the percentage of MCSs should remain constant. Thus, our finding that the percentage of MSSs remained unchanged after fear conditioning (Figure 4G) suggests that new boutons tend to replace old ones, which would represent supplanting of old connectivity patterns by new ones. In contrast, the significant increase in the number of MSBs that results from fear conditioning (Figure 4F) suggests that new spines are added to existing synapses without eliminating old ones, representing addition of new connections while preserving old ones.

We generated a mathematical model based on MSB/MSS percentages and the *in vivo* bouton/spine turnover results to quantitatively assess the difference in the turnover pattern of boutons and spines. Specifically, seeking to estimate the proportions of newly formed boutons/spines being replaced (replacement) and/or added (addition) during synaptic turnover, we developed a combinatorial mathematical model that exhausted all turnover possibilities based on results from ssEM and *in vivo* imaging (Figure 5C and 5D). We used the model to estimate: 1) the proportion of boutons/spines for which formation was accompanied by elimination, and 2) the proportion of boutons/spines that are simply added to existing synapses without eliminating old ones.

We took the MCS/1-to-1 synapse composition of control mice as the starting situation and that of conditioned mice as the end situation, using a bipartite graph to model synaptic connections. In order to better reflect the difference in the MSB ratio

before and after learning, as well as to take into account computational complexity, we modeled using 120 synapses to obtain the final expected values, using combinatorics to calculate the possibility of different patterns. We assumed an equal possibility for all turnover patterns. The percentages of MSBs and MSSs, and the elimination and formation rates of spines and boutons were all based on experimental data (Figure 4F, 4G and 5B). Synaptic turnover patterns that involve newly formed boutons/spines include the following 6 categories ('-' represents elimination and '+' formation):

$$\text{synaptic turnover (involving formation):} \begin{cases} \text{1-to-1 synapse} \rightarrow \text{1-to-1 synapse: } -1 \text{ and } +1 \text{ (A.)} \\ \text{multiple-contact synapse} \rightarrow \text{1-to-1 synapse: } -2 \text{ and } +1 \text{ (B.)} \\ \text{1-to-1 synapse} \rightarrow \text{multiple-contact synapse:} \begin{cases} -0 \text{ and } +1 \text{ (C.)} \\ -1 \text{ and } +2 \text{ (D.)} \end{cases} \\ \text{multiple-contact synapse} \rightarrow \text{multiple-contact synapse:} \begin{cases} -1 \text{ and } +1 \text{ (E.)} \\ -2 \text{ and } +2 \text{ (F.)} \end{cases} \end{cases}$$

According to the above classification, "synaptic competition" includes (A.), (B.), (D.), (E.) and (F.), and "synaptic addition" includes only (C.). We built two models, one for bouton turnover and MSS, the other for spine turnover and MSB. These two models can each capture bouton and spine turnover patterns (for detailed calculation, see the Methods).

Our combinatorial mathematical modeling predicts a much higher percentage of competition of boutons than that of spines (Figure 5E, 5G and 5H, Methods), which is consistent with our observation *in vivo*: among 856 putative synapses identified from two-photon imaging of the A1 (Methods), there were 9 cases of a new bouton replacing an old bouton, and 4 cases of a new spine adding onto an existing synapse; there were no cases wherein a new bouton was added to an existing synapse (Figure 5F). Note that we attribute the low frequency of turnover events of MCSs present in our *in vivo* dataset to the sparseness of neuronal labeling. Together, these data suggest that each bouton tends to be the sole input of its postsynaptic counterpart, whereas spines can co-exist on a single bouton.

Evaluating the information storage capacity of MSBs in static synaptic networks

Compared to two 1-to-1 synapses, two synapses formed by one MSB saved cellular resources required for two distinct presynaptic boutons. To investigate the information coding capacity of MSBs, we developed a mathematical model to calculate the information storage capacity (ISC)[28-31] of a synaptic network comprising a set number of synaptic connections. The ISC of a synaptic network is given by the Shannon's information entropy $H32$, which measures the average uncertainty in the synaptic connection patterns of the network, and can be expressed as:

$$H(X) = E[-log_2 p(x)] = -\sum_{i=1}^{n} p(x_i) log_2 p(x_i)\,,$$

where, n is the number of all possible connection patterns, X is a random variable of synaptic connection patterns, $p(x)$ is the probability mass function of X, and $p(x_i)$ is the probability measure of the occurrence of the ith synaptic connection pattern x_i. We assume that the probability of each pattern of synaptic connection is equal, then the model transforms into a mode to solve for the number of eligible patterns. Here, the degree of uncertainty in the network depends on the number of available dendrites to which each bouton could connect to. For cases where the multiple postsynaptic structures of one MSB originate from the same dendrite, we consider the connection to be the same as a 1-to-1 synapse. Therefore, the ISC of an MSB synapse is determined by how many dendrites that the MSB connects to.

To determine the number of available dendrites for each bouton and the percentages of both single-dendritic and multi-dendritic MSBs, we used the Multicut pipeline[33] and performed saturated reconstruction for two A1 tissue blocks of one control (22 × 24 × 25 μm) and one conditioned (33 × 28 × 25 μm) mouse (Figure 6A, Supp. Video 2-5, Extended Data Figure 9, Methods). Since the typical length of a spine is 1-μm34, we calculated the number of dendrites passing the vicinity of a bouton within a 1-μm radius in the reconstructed data set (Figure 6C, Supp. Video 6, Methods). Among the 5,774 boutons analyzed (Methods, Figure S10), the median number of potential postsynaptic dendrites was 9 (Figure 6D), indicating that each bouton can potentially make synapse with 9 dendrites. We also traced each spine to its original dendrite to support categorization of MSB subtypes. Contrary to previous *in vitro* results reporting that LTP can lead to single-dendritic MSB—and thereby generating stronger connections between pre- and post-synaptic neurons[35]—we found that more than 90% of MSBs were connected to multiple dendrites (Figure 6B), forming 1-to-N connections.

We then calculated the ISC of the synaptic network based on the synapse reconstruction results containing different types of connections: 1) 1-to-1 synapses only; 2) 1-to-1 synapses and single-dendritic MSBs; 3) 1-to-1 synapses, single- and multi-dendritic MSBs (Figure 6E). In a model with 100 synapses, of which 6% are MSB synapses (Figure 4F), single-dendritic MSB increased ISC by 2.5% over 1-to-1 synapses, and multi-dendritic MSB further added 2.2%. The benefits of adding MSBs remained when the model was scaled up to 10^6 synapses (Figure 6G, Methods). These results indicate that MSBs in a static network do increase information coding capacity, but only slightly.

A plastic connectivity model for the information storage capacity of synaptic networks

The percentage of multi-dendritic MSBs among all MSBs was higher in the conditioned mouse (95.1%) than in the control mouse (87.0%). This result, together with the percentages of MSBs in control and conditioned mice (5.0 ± 0.3% vs. 6.8 ± 0.2%, Figure 4F), indicates that essentially all of the MSBs newly formed after fear conditioning were multi-dendritic. Thus, fear conditioning resulted in boutons making novel connections with other dendrites, rather than strengthening existing connections.

To evaluate the difference in ISC from establishment of new synaptic connections under the two conditions, multi-dendritic vs. single-dendritic, we built a synaptic network model that incorporated synaptic plasticity by adding 10% more spines to the boutons (Figure 6F), based on the *in vivo* imaging results (Figure 5B). The increase in ISC depends on the number of new connections formed, and the number of potential connection targets for each new connection. For newly formed multi-dendritic connections, the number of potential targets for each new connection is the number of dendrites surrounding a bouton (Figure 6D; condition A, forming multi-dendritic MSB); for single-dendritic, the number of potential target is 1 (condition B, forming single-dendritic MSB).

The changes in ISC due to this 10% addition of synapses in the network, denoted by the increase of information entropy ΔH, were calculated for the condition A and condition B as follows:

$$\Delta H = H(Y) - H(X) = E[-log_2 p(y)] - E[-log_2 p(x)]$$
$$= -\sum_{i=1}^{m} p(y_i) log_2 p(y_i) - \left(-\sum_{i=1}^{n} p(x_i) log_2 p(x_i) \right),$$

where, n and m are the number of all synaptic connection patterns before and after formation, respectively; Y and X are the random variables of the connection patterns after and before formation, respectively; $p(y)$ and $p(x)$ are the probability mass functions of Y and X, respectively; $p(y_i)$ is the probability of occurrence of the ith synaptic connection pattern after formation y_i; $p(x_i)$ is the probability of the ith connection pattern before formation x_i. We assume that the probability of each possible connection pattern is equal, the above dynamic model can also transform into a mode to solve for the number of eligible patterns.

Notably, whereas a multi-dendritic MSB only slightly adds to the ISC in a static network (Figure 6G), in this plastic network, the increase in ISC for condition A was more than 50% higher (Figure 6H) than that of condition B. And we found that this relative advantage for multi-dendritic connectivity scaled linearly with network size (Figure 6I).

Discussion

It is well-established that learning can induce neuronal plasticity in the brain. In previous *in vivo* imaging studies, only a limited population of synapses were investigated, and it is not known how learning changes the shape and size of mitochondria in the brain. In this study, we used deep learning techniques to automatically detect synapses and mitochondria in ssEM images (Extended Data Figure 2). This method allowed us to examine hundreds of thousands of synapses and mitochondria, and our results demonstrated that synaptic and mitochondrial organization were significantly affected by the learning process. With a particular focus on synapses consisting of multiple synaptic elements, we were able to identify a specific form of MCSs consisting of a single bouton and multiple spines from different dendrites, which were indicated by mathematical modeling to confer higher information storage than single-contact synapses.

In this paper, we proposed a novel 2D-3D pipeline to outline the 3D morphology of synapses and mitochondria from ssEM images. The first step focused on detecting and segmenting instances on 2D slices with advanced R-CNN. The second step converted the 2D instances into 3D individuals, mainly based on the similarity index of adjacent layers. Compared with other CNN techniques, the experimental results demonstrated that our method greatly improved performance. This pipeline can potentially be used to identify any cellular compartment or organelle with distinct structural properties. Apart from PSD, vesicles are an important feature to help identify synapses from ssEM images. The SyConn framework[10] designed a multiclass CNN to learn the co-occurrence of synaptic junctions and vesicle clouds. How to combine information from vesicles to enhance detection of the synaptic cleft is a possible future research direction. As for the detection of MCSs, we first located them based on close-proximity criterion. Then, presynaptic vesicle information was introduced to classify MSBs and MSSs. After that, we obtained the dense reconstruction results by solving the graph partitioning problem. The origination of multiple elements of MSBs or MSSs can be traced according to the dense reconstructions. This is the first report of detecting MCSs using vesicle and neuronal segmentation results. However, the inherent error of our MCS detection algorithm is a limitation of this study. Predicting the synaptic partner neurons using CNNs may be a solution in the future.

Dendritic spines have been extensively studied by *in vivo* imaging methods, because their unique shape makes them easily identifiable. However, there are also synapses formed on dendritic shafts, which are not visible by fluorescent imaging. They can, however, be easily identified using our synapse classifier (Methods) algorithms from ssEM images. In fact, 26% of all identified synapses were shaft synapses (Extended Data Figure 7C), and after learning, their number decreased as spine synapses increased (Extended Data Figure 7A and 7B), ultimately resulting in an unaltered total number of synapses. These synapses likely contribute to the homeostasis of cellular resource relocation and synapse organization.

The ssEM method enabled us to identify a special type of synapse, namely the multiple-contact synapses. Our previous work[3] indicated that most new synapses are formed by adding a synaptic element, either a presynaptic bouton or postsynaptic spine, to an existing synapse. We called this the "partial addition rule". Adding a bouton to an existing synapse creates an MSS, while adding a spine creates an MSB. We found that both the MSB number and proportion increased significantly after learning, but MSS stayed the same. Since bouton formation and spine formation both increased after learning, this result suggested that a new bouton was more likely to compete and oust the previous bouton in a synapse for being the sole input to a postsynaptic spine, while the new spine and the old spine could co-exist on a single bouton, leading to a higher proportion of MSBs. MSS synapses may remain in a transient state during the switch from an old synaptic contact to a new one, while MSB represents a more stable synaptic configuration, allowing simultaneous information transfer from a single bouton to multiple postsynaptic sites. For any MSS, boutons from different neurons likely have unsynchronized activities, and only one of them would correlate best with the MSS. According to the Hebbian postulate "fire together, wire together", only the best correlated bouton will win the competition to be the sole input for the spine, and the MSS will turn into a single-synaptic spine.

In most cases, the transmitters released from presynaptic sites outnumber the postsynaptic receptors, so it is efficient to transmit information from one bouton to multiple postsynaptic targets. Indeed, most MSBs made contact with more than one dendritic branch, broadcasting information from one neuron to multiple neurons with one multiple-contact bouton, with minimal cellular energy consumed. We noted that the proportion of MSB is very low, consistent with the notion that memory encoding may be very sparse. For any piece of memory, only very few synapses are involved in coding the information. Our model indicated a 50% increase in information storage capacity for multi-dendritic MSBs, which provides great potential for synaptic plasticity with minimal increase of synapse number and structures.

Mitochondria adapt to the cellular energy requirements by highly dynamic fusion and fission[36]. Mitochondrial dynamics are also found to be related to synaptic transmission and plasticity. There is evidence to suggest that increasing mitochondrial fragments can promote synapse formation[37]. Our results show significant decrease in size and increase in number of mitochondria along with changes of synaptic organization following fear conditioning, suggesting that mitochondria may play a role in learning by balanced fusion and fission.

The recently reported connectome of $1 mm^3$ human cerebral cortex[11] shows the substantial improvement of EM imaging speed and the powerful ability of deep learning. Similar to our work, they found many strong (multi-synaptic) connections on both excitatory and inhibitory neurons. The biggest difference is that rather than performing large-scale saturated reconstruction, we conducted specific and local classification of synapses and mitochondria, which allows ultra-structural analyses of specific cellular organelles without resource-demanding heavy computation. As our method applies

region-based CNN to identify objects, it can potentially be used to extract other discrete, distinct structures from ssEM data as well, such as Golgi apparatus and nucleus, making it a versatile tool for ssEM image processing.

Acknowledgments

We thank Drs. Mu-ming Poo, Ju Lu, Yi Zuo and Margaret S. Ho for critical comments and suggestions. We also thank Linlin Li, Lina Zhang and Jingbin Yuan for technical support; Jie Luo, Jiazheng Liu, Yi Jiang and Lu Wang for manual proofreading. This work was supported by grants from the Ministry of Science and Technology of China (2018YFC1005004) and the Natural Science Foundation of China (31970960) to Y.Y., the Strategic Priority Research Program of CAS (XDB32030200), Bureau of International Cooperation, CAS (153D31KYSB20170059) to H.H., and the Natural Science Foundation of China (61673381) to Q-w. X.

Author contribution

H.H., Q.X. and Y.Y. conceived and guided the project. J.Q., Y.Y. and Y.K. performed the animal experiments and provided the samples. H.M. conducted EM imaging. G.L. implemented automated location and navigation system. X.C. performed alignment. J.L. and B.H. developed the algorithms. Z.L. established the mathematical models. L.S. performed visualization. Y.Y., J.L., J.Q. and Z.L. wrote the manuscript with contributions from all authors.

Declaration of Interests

The authors declare no competing interests.

References

1. Xu, T., et al., *Rapid formation and selective stabilization of synapses for enduring motor memories.* Nature, 2009. **462**(7275): p. 915-919.
2. Yang, G., F. Pan, and W.-B. Gan, *Stably maintained dendritic spines are associated with lifelong memories.* Nature, 2009. **462**(7275): p. 920-924.
3. Yang, Y., et al., *Selective synaptic remodeling of amygdalocortical connections associated with fear memory.* Nature Neuroscience, 2016. **19**(10): p. 1348-1355.
4. Schoonover, C.E., et al., *Comparative strength and dendritic organization of thalamocortical and corticocortical synapses onto excitatory layer 4 neurons.* Journal of Neuroscience, 2014. **34**(20): p. 6746-6758.
5. Hayworth, K.J., et al., *Imaging ATUM ultrathin section libraries with WaferMapper: a multi-scale approach to EM reconstruction of neural circuits.* Frontiers in Neural Circuits, 2014. **8**: p. 68.

6. Mishchenko, Y., et al., *Ultrastructural analysis of hippocampal neuropil from the connectomics perspective.* Neuron, 2010. **67**(6): p. 1009-1020.
7. Staffler, B., et al., *SynEM, automated synapse detection for connectomics.* Elife, 2017. **6**: p. e26414.
8. Jagadeesh, V., et al., *Synapse classification and localization in electron micrographs.* Pattern Recognition Letters, 2014. **43**: p. 17-24.
9. Kreshuk, A., et al. *Automated segmentation of synapses in 3D EM data*. in *2011 IEEE International Symposium on Biomedical Imaging: From Nano to Macro*. 2011. IEEE.
10. Dorkenwald, S., et al., *Automated synaptic connectivity inference for volume electron microscopy.* Nature Methods, 2017. **14**(4): p. 435-442.
11. Shapson-Coe, A., et al., *A connectomic study of a petascale fragment of human cerebral cortex.* bioRxiv, 2021.
12. Friedman, J.R. and J. Nunnari, *Mitochondrial form and function.* Nature, 2014. **505**(7483): p. 335-343.
13. Vos, M., E. Lauwers, and P. Verstreken, *Synaptic Mitochondria in Synaptic Transmission and Organization of Vesicle Pools in Health and Disease.* Frontiers in Synaptic Neuroscience, 2010. **2**(139).
14. Lucchi, A., et al. *Exploiting enclosing membranes and contextual cues for mitochondria segmentation*. in *International Conference on Medical Image Computing and Computer-Assisted Intervention*. 2014. Springer.
15. Lucchi, A., et al., *Supervoxel-based segmentation of mitochondria in em image stacks with learned shape features.* IEEE Transactions on Medical Imaging, 2011. **31**(2): p. 474-486.
16. Narasimha, R., et al., *Automatic joint classification and segmentation of whole cell 3D images.* Pattern Recognition, 2009. **42**(6): p. 1067-1079.
17. Oztel, I., et al. *Mitochondria segmentation in electron microscopy volumes using deep convolutional neural network.* in *2017 IEEE International Conference on Bioinformatics and Biomedicine (BIBM)*. 2017. IEEE.
18. He, K., et al. *Mask r-cnn*. in *Proceedings of the IEEE international conference on computer vision*. 2017.
19. Lin, T.-Y., et al. *Feature pyramid networks for object detection*. in *Proceedings of the IEEE conference on computer vision and pattern recognition*. 2017.
20. He, K., et al. *Deep residual learning for image recognition*. in *Proceedings of the IEEE conference on computer vision and pattern recognition*. 2016.
21. Ronneberger, O., P. Fischer, and T. Brox. *U-net: Convolutional networks for biomedical image segmentation*. in *International Conference on Medical image computing and computer-assisted intervention*. 2015. Springer.
22. Çiçek, Ö., et al. *3D U-Net: learning dense volumetric segmentation from sparse annotation*. in *International Conference on Medical Image Computing and Computer-Assisted Intervention*. 2016. Springer.
23. Quan, T.M., D.G. Hildebrand, and W.-K. Jeong, *Fusionnet: A deep fully residual convolutional neural network for image segmentation in connectomics.* arXiv preprint arXiv:.05360, 2016.

24. Jones, T.A., et al., *Induction of multiple synapses by experience in the visual cortex of adult rats.* Neurobiology of Learning, 1997. **68**(1): p. 13-20.
25. Sorra, K. and K.M. Harris, *Occurrence and three-dimensional structure of multiple synapses between individual radiatum axons and their target pyramidal cells in hippocampal area CA1*. Journal of Neuroscience, 1993. **13**(9): p. 3736-3748.
26. Woolley, C.S., H.J. Wenzel, and P.A. Schwartzkroin, *Estradiol increases the frequency of multiple synapse boutons in the hippocampal CA1 region of the adult female rat.* Journal of Comparative Neurology, 1996. **373**(1): p. 108-117.
27. Geinisman, Y., et al., *Associative learning elicits the formation of multiple-synapse boutons.* Journal of Neuroscience, 2001. **21**(15): p. 5568-5573.
28. Chklovskii, D.B., B. Mel, and K. Svoboda, *Cortical rewiring and information storage.* Nature, 2004. **431**(7010): p. 782-788.
29. Escobar, G., T. Fares, and A. Stepanyants, *Structural plasticity of circuits in cortical neuropil.* Journal of Neuroscience, 2008. **28**(34): p. 8477-8488.
30. Stepanyants, A. and G. Escobar, *Statistical traces of long-term memories stored in strengths and patterns of synaptic connections.* Journal of Neuroscience, 2011. **31**(21): p. 7657-7669.
31. Stepanyants, A., P.R. Hof, and D.B. Chklovskii, *Geometry and structural plasticity of synaptic connectivity.* Neuron, 2002. **34**(2): p. 275-288.
32. Shannon, C.E., *A mathematical theory of communication.* The Bell System Technical Journal, 1948. **27**(3): p. 379-423.
33. Beier, T., et al., *Multicut brings automated neurite segmentation closer to human performance.* Nature methods, 2017. **14**(2): p. 101-102.
34. Bai, W., et al., *Automatic dendritic spine analysis in two photon laser scanning microscopy images.* Cytometry Part A, 2007. **71A**.
35. Polsky, A., B.W. Mel, and J. Schiller, *Computational subunits in thin dendrites of pyramidal cells.* Nature Neuroscience, 2004. **7**(6): p. 621-627.
36. Westermann, B., *Bioenergetic role of mitochondrial fusion and fission.* Biochimica et Biophysica Acta (BBA)-Bioenergetics, 2012. **1817**(10): p. 1833-1838.
37. Dickey, A.S. and S. Strack, *PKA/AKAP1 and PP2A/Bβ2 regulate neuronal morphogenesis via Drp1 phosphorylation and mitochondrial bioenergetics.* Journal of Neuroscience, 2011. **31**(44): p. 15716-15726.
38. Chen, X., et al. *Morphology-retained non-linear image registration of serial electron microscopy sections*. in *2018 25th IEEE International Conference on Image Processing (ICIP)*. 2018. IEEE.
39. Liu, C., J. Yuen, and A. Torralba, *Sift flow: Dense correspondence across scenes and its applications.* IEEE Transactions on Pattern Analysis and Machine Intelligence, 2010. **33**(5): p. 978-994.
40. Schaefer, S., T. McPhail, and J. Warren, *Image deformation using moving least squares*, in *ACM SIGGRAPH 2006 Papers*. 2006. p. 533-540.
41. Abadi, M., et al. *Tensorflow: A system for large-scale machine learning*. in *12th {USENIX} symposium on operating systems design and implementation ({OSDI}*

16). 2016.

42. Bottou, L., *Stochastic gradient descent tricks*, in *Neural networks: Tricks of the trade*. 2012, Springer. p. 421-436.
43. Peters, A., K. Josephson, and S.L. Vincent, *Effects of aging on the neuroglial cells and pericytes within area 17 of the rhesus monkey cerebral cortex.* The Anatomical Record, 1991. **229**(3): p. 384-398.
44. Bourne, J.N. and K.M. Harris, *Coordination of size and number of excitatory and inhibitory synapses results in a balanced structural plasticity along mature hippocampal CA1 dendrites during LTP.* Hippocampus, 2011. **21**(4): p. 354-373.

Figure legends

Figure 1. Overall schematic of the experimental procedure.
(A) Auditory fear conditioning and sample preparation. Control mice are subjected to 5 sessions of single tone pip delivery; conditioned mice are subjected to 5 sessions of paired tone pip and foot shock delivery. At 4 days after conditioning, auditory cortex (A1) tissue blocks are harvested from these mice and prepared for serial section electron microscopy (ssEM).
(B) The ssEM image acquisition and alignment procedure. Serial sections are automatically sectioned using automated tape-collecting ultramicrotome (ATUM); these are collected onto 4-inch silicon wafers. The wafers are then imaged using scanning electron microscopy. Raw images are aligned using a SIFT-flow-based, non-linear registration algorithm.
(C) Identification of synapses and mitochondria in A1. Synapses and mitochondria are automatically identified using our 2D-3D pipeline based on Region-Convolutional Neural Network (R-CNN).
(D) The reconstructed dendrites from the saturated reconstruction by applying the Multicut pipeline[33]. The spine fragments are manually traced to the original dendrite.
(E) MCSs localization and classification. Multiple-contact synapses (MCSs) are manually located and then classified into Multi-Synaptic Boutons (MSBs, those consisting of a single bouton contacting multiple postsynaptic sites) and Multi-synaptic Spines (MSSs, those consisting of a single spine contacting multiple boutons) by incorporating the vesicle cloud features.
(F) Comparative statistical analysis and mathematical modeling. A combinatorial mathematical model is built to simulate the synaptic turnover associated with the fear conditioning process.
(G) MSB subtypes. MSBs are classified into single- or multi- dendritic MSBs by incorporating saturated reconstructions to identify the origination dendrites of multiple postsynaptic spines.
(H) Comparative statistical analysis and synaptic connectivity modeling. A synaptic network is built by connecting the axon and potential dendrite pairs within a 1-μm radius sphere around a bouton.

Figure 2. Automated identification and reconstruction of synapses.
(A) Examples of an EM image and a binary synaptic mask predicted by Mask R-CNN. Scale bar: 1 μm.
(B) Network architecture of Mask R-CNN, which takes a 1,024×1,024 image patch as input and outputs the bounding boxes (golden box) and binary masks (orange box) of all synapses in the input image

(C) Sketch of the similarity-index-based 3D connection algorithm used for reconstructing synapses. The similarity of two synapses from adjacent layers depends on the intersection-over-union of the bounding boxes.

(D) Normalized histograms of Euclidean distances between any two synapses in control (blue) and conditioned mice (red); note that these accord with a normal distribution (control: $p = 0.1149$, two-sided Kolmogorov-Smirnov test, conditioned: $p = 0.4801$, two-sided Kolmogorov-Smirnov test).
(E) Comparison with other state-of-the-art methods in terms of precision, recall, and F1-score metrics on a public ssEM dataset. Each circle indicates an image from the test sets (half of this public ssEM dataset).
(F) Comparison with other automatic state-of-the-art CNN methods as well as manual annotation on computation efficiency, which was here evaluated as the number of voxels processed per day. With one GPU, R-CNN (golden) is in the same order of magnitude as 3D U-Net (red), one order of magnitude faster than U-Net (blue), and two orders of magnitude faster than manual processing by humans (purple).

Figure 3. Automated identification of mitochondria and vesicle clouds.
(A) Examples of an EM image and a binary mitochondrial mask predicted by Mask R-CNN. Scale bar: 1 μm.
(B) EM image and 3D visualization of 8 mitochondria located in dendrites or axons. Scale bar: 1 μm.
(C) 3D visualizations of all mitochondria from one 22 × 24 × 25 μm image stack.
(D) The mitochondrial volume is smaller in conditioned mice ($0.08\pm0.001\ \mu m^3$) than in controls ($0.11\pm0.003\ \mu m^3$). $p < 0.01$, two-sided t-test.
(E) The mitochondrial density is higher in conditioned mice ($0.65\pm0.014\ \mu m^3$) than in controls ($0.57\pm0.023\ \mu m^3$). $p < 0.01$, two-sided t-test.
(F) The postsynaptic density (PSD) area with mitochondria in presynaptic boutons ($0.21\pm0.008\ \mu m^2$) is larger than the PSD area without mitochondria in presynaptic boutons ($0.12\pm0.002\ \mu m^2$). $p < 0.001$, two-sided t-test.
(G) Typical example of a spine synapse with the identified PSD (green), mitochondria (red) and vesicle cloud (purple). Another view and the corresponding EM images are displayed on the right. Scale bar: 1 μm.

Figure 4. Synaptic organization in A1.
(A) MCSs detection and classification. MCS candidates are first automatically marked based on a close-vicinity criterion, and are then manually verified and classified as MSBs or MSSs by estimating the number of boutons based on vesicle cloud segmentation. Specifically, the bouton number is estimated by intersecting the fitting circle of synapse and bounding box of vesicle cloud. Neurite reconstructions are then introduced to determine the origination of multiple spines or boutons. Red circles: fitted circles by synapse segmentation; Green boxes: minimum boundary rectangles of vesicle cloud segmentation. Scale bar: 1 μm.
(B) Two examples of false positives that were identified after 3D reconstruction of synapses. The lefthand subpanel is an MSB false positive that was falsely detected owing to the horse shoe-shaped bouton (dark green). The righthand subpanel is an MSS false positive comprising two shaft synapses. Scale bar: 1 μm.
(C-E) Examples of a 3D reconstructed MSB (A), an MSB with more than 2 postsynaptic

sites (B), and an MSS (C). Scale bar: 1 μm.
(F) The percentage of MSB synapses is higher in conditioned mice (6.8±0.2 %) than in controls (5.0±0.3 %). $p < 0.01$, two-sided t-test.
(G) There is no difference in the percentage of MSS synapses between control (1.8±0.4 %) and conditioned mice (1.4±0.4 %). $p = 0.46$, two-sided t-test.
(H) The percentage of MSB synapses with presynaptic mitochondria (59.41±1.3%) is higher than the percentage of SSB synapses with presynaptic mitochondria (34.12±0.6%). $p < 0.001$, two-sided t-test.

Figure 6. Synaptic turnover patterns.
(A) Cartoons showing competition and addition in bouton and spine turnover.
(B) Turnover rates of spines (formation: 9.71±1.02 %, elimination: 8.93±0.41 %) and boutons (formation:14.73±1.03 %, elimination: 17.76±1.24 %) in the auditory cortex of fear conditioned mice. Each circle represents data from a single mouse. The bouton turnover rate is averaged among axons that project to the auditory cortex from the lateral amygdala (LA), the anterior cingulate cortex (ACC), and the medial geniculate nucleus (MGN).
(C-D) Diagram showing spine and bouton turnover in combinatorial mathematical models. Model for bouton (green) turnover (C). Model for spine (purple) turnover (D). white: eliminated spine/bouton; yellow: added new spine/bouton; arrow: synaptic connection.
(E) Estimation of the percentage of competition and addition for boutons (left) and spines (right) based on combinatorial mathematical modeling. Models predict 95.4% competition of boutons and 73.2% competition of spines.
(F) Synaptic turnover examples from *in vivo* two-photon microscopy anlaysis. Arrows point to elimination of an old bouton and to formation of a new bouton (top), and to an addition of a new spine (bottom). Scale bar: 1 μm.
(G) The percentage of competition in bouton turnover is maintained around 96% when the model size is scaled up to 12,000 synapses.
(H) The percentage of competition in spine turnover is maintained around 72% when model size is scaled up to 12,000 synapses.

Figure 7. Saturated reconstruction and information storage capacity calculation.
(A) Two reconstructed tissue blocks from control (left: 22 × 24 × 25 μm) and conditioned mice (right: 33 × 28 × 25 μm). Insets show examples of single- or multi-dendritic MSBs. Scale bar: 1 μm.
(B) Percentage of single- and multi-dendritic MSBs in control (multi-dendrite MSBs: 86%) and conditioned mice (multi-dendrite MSBs: 95%).
(C) A reconstructed example showing 10 dendrites intersecting within a 1μm radius of a bouton. Scale bar: 1 μm.
(D) Distribution of the number of dendrites within a 1-μm radius of a bouton. $n = 5774$ boutons.
(E) Illustrations showing synaptic connectivity patterns of a static model. Condition 1: 1-to-1 synapses only; condition 2: 1-to-1 synapses and single-dendritic MSBs;

condition 3: 1-to-1 synapses, single- and multi-dendritic MSBs.
(F) Illustrations showing synaptic connectivity patterns of a dynamic model. Condition A: multi-dendritic MSBs, condition B: single-dendritic MSB only. Red: dendrite; green: bouton; solid arrow: one possible synaptic connection; dashed arrow: potential synaptic connection.
(G) Information storage capacity (ISC) for static networks of different sizes for 3 conditions: 1-to-1 synapses only (condition 1); 1-to-1 synapses and single-dendritic MSBs (condition 2); 1-to-1 synapses, single- and multi-dendritic MSBs (condition 3).
(H) Increase in ISC for dynamic networks of different sizes for 2 conditions: new synapse on any passing dendrite (condition A); new synapse on the same dendrite (condition B).
(I) Linear relationship for the increase in ISC for conditions A and B across different network sizes.

Figure 1

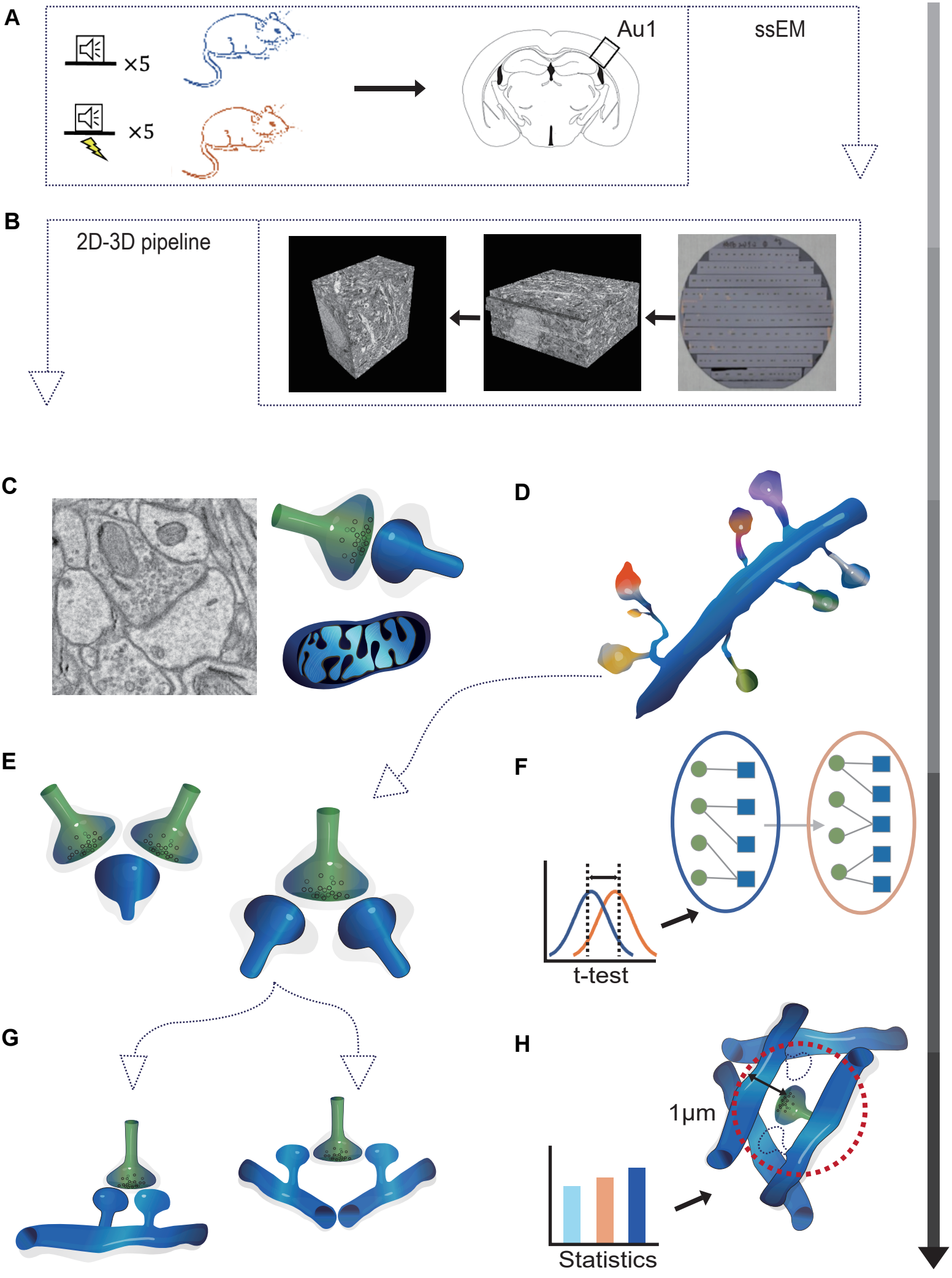

Figure 2

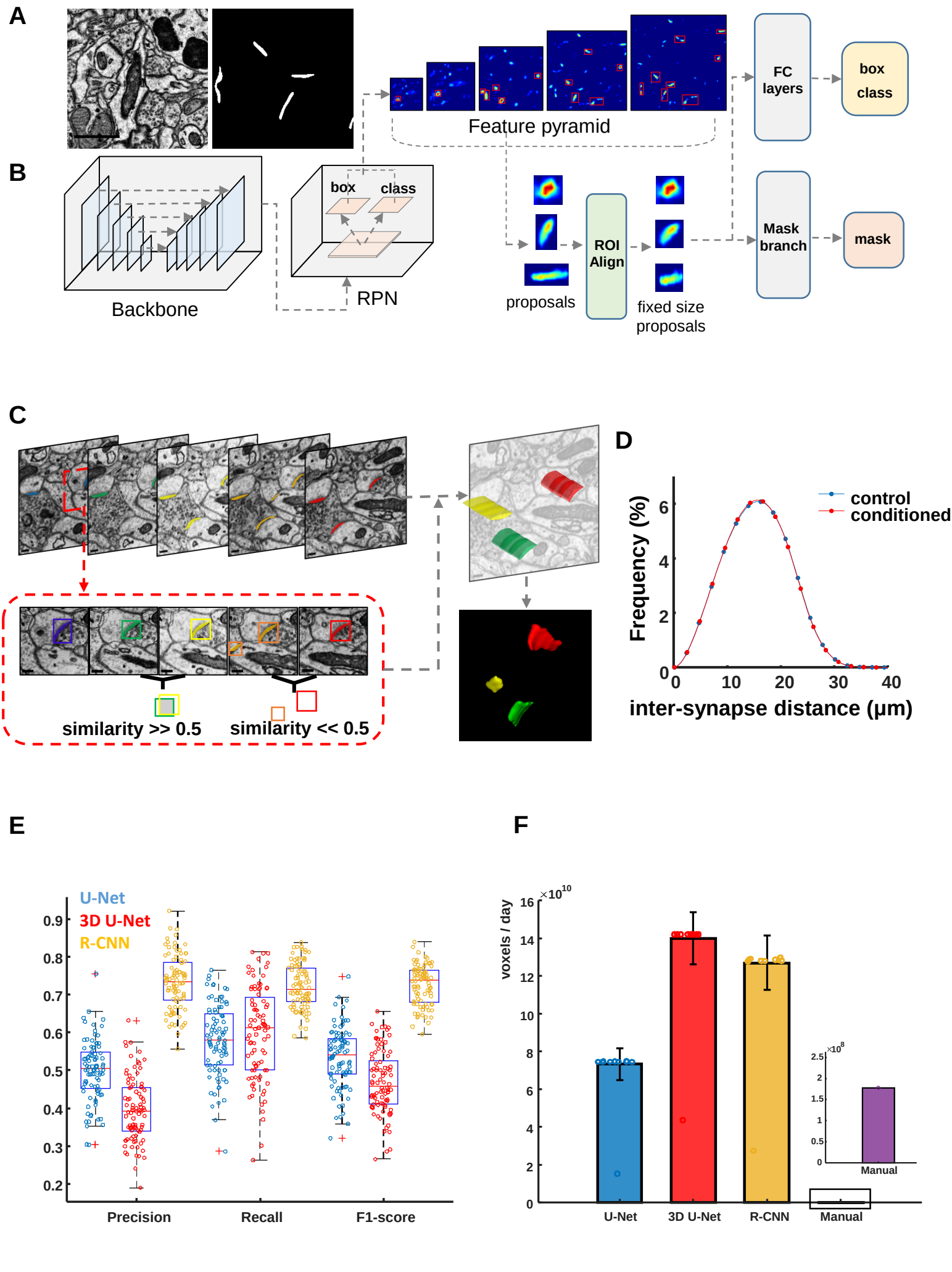

Figure 3

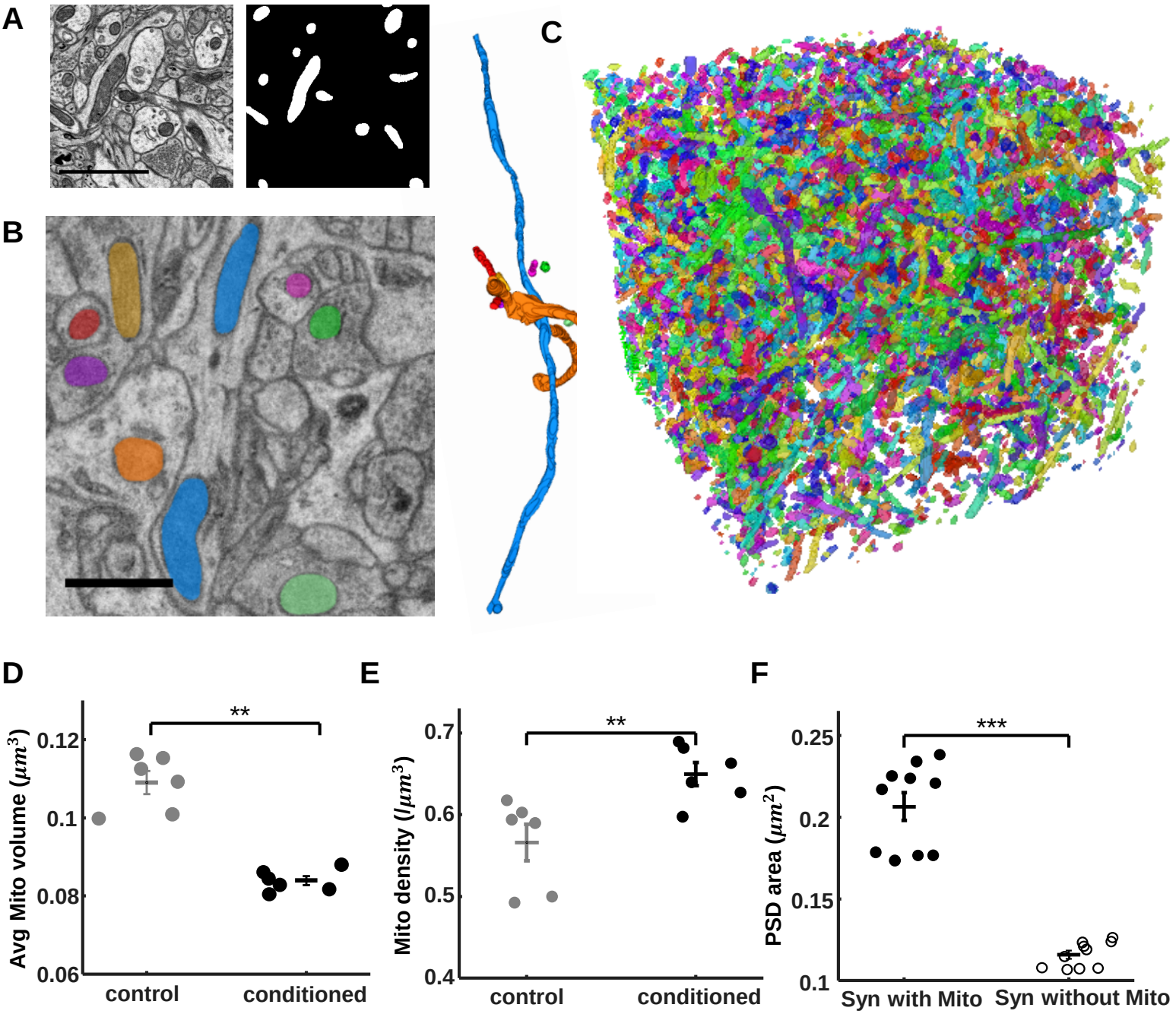

Figure 4

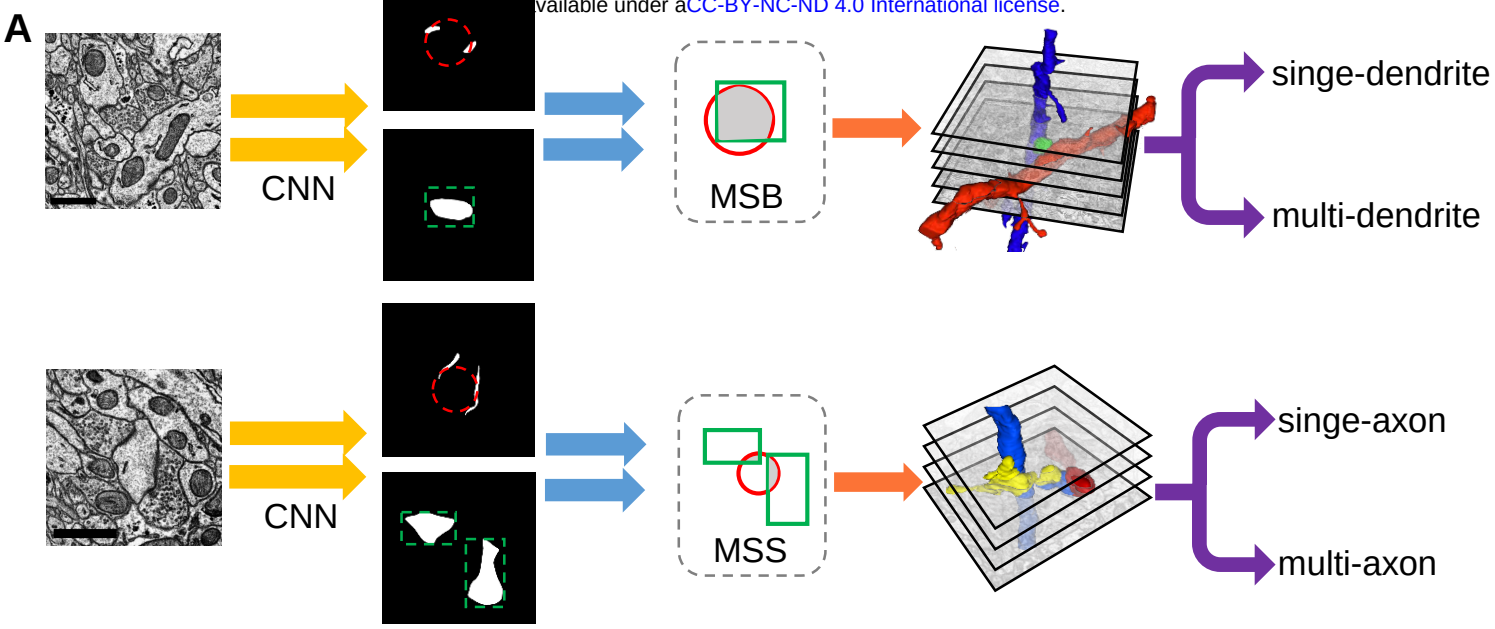

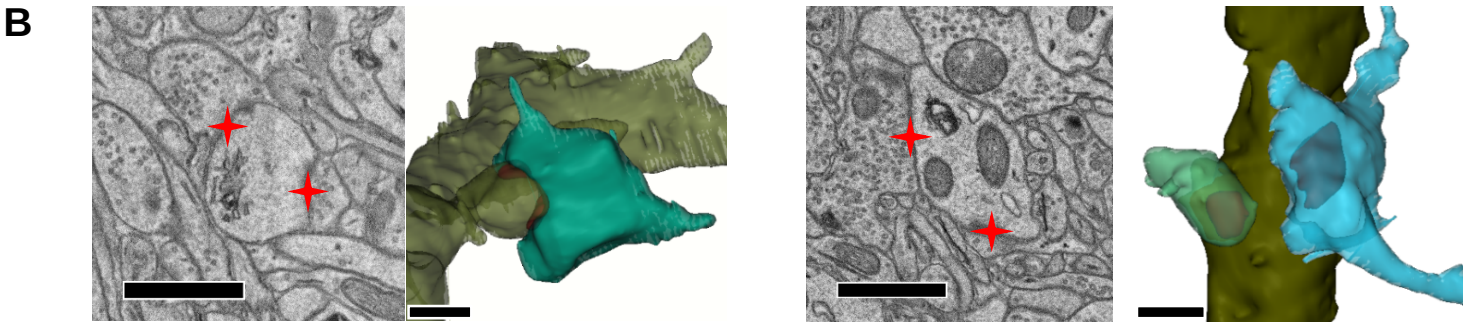

A horse shoe-shaped bouton
(MSB False Positive)

Shaft synapses on one plane
(MSS False Positive)

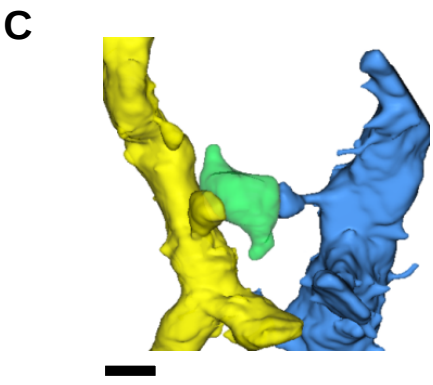

Multi-synapse bouton

Multi-synapse bouton with 3 synapses

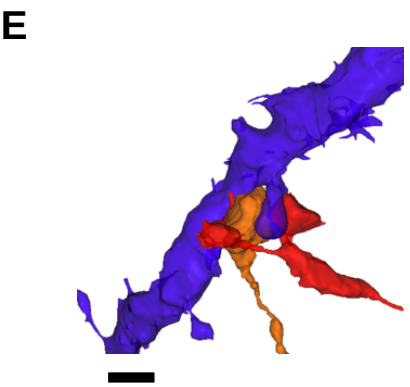

Multi-synapse spine

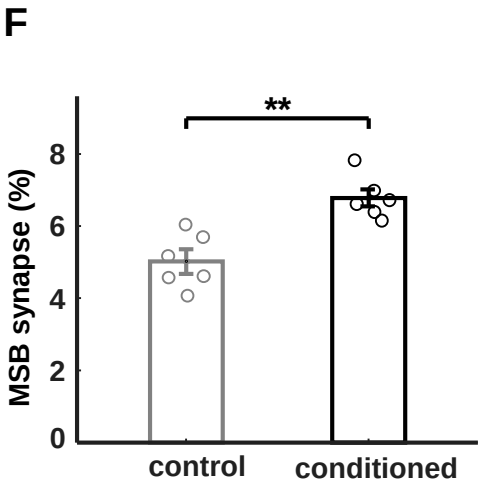

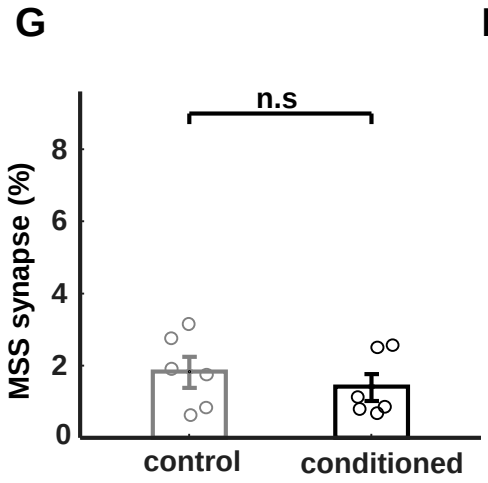

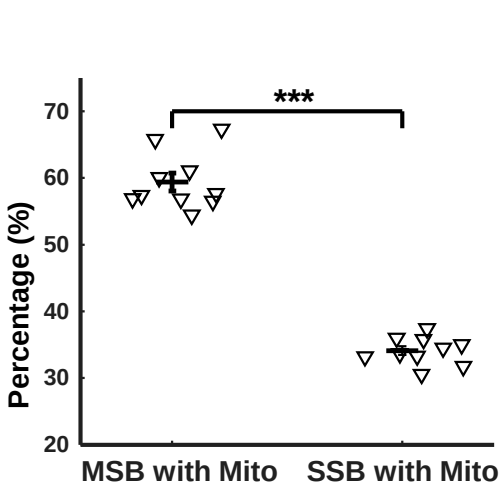

Figure 5

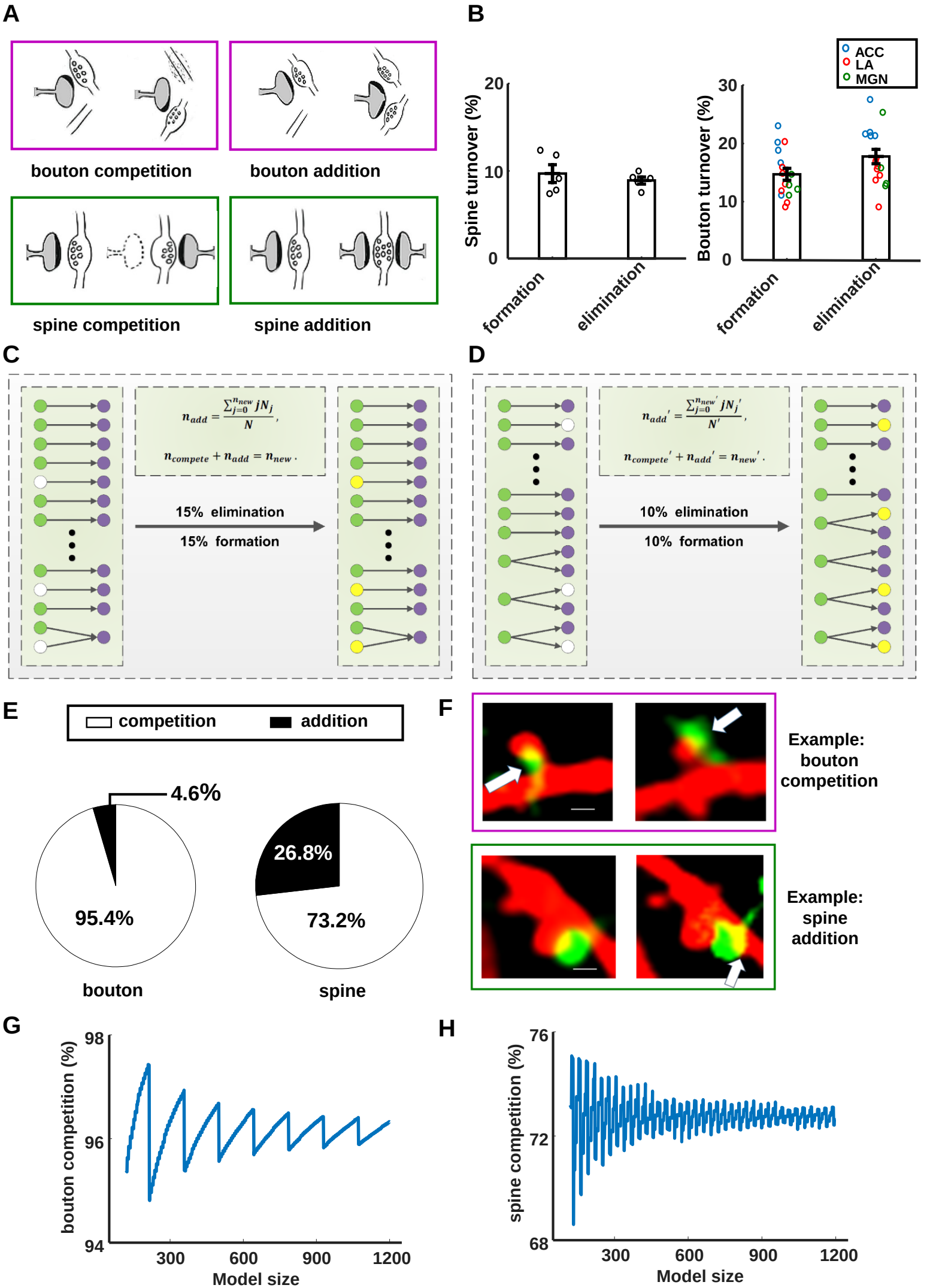

Figure 6

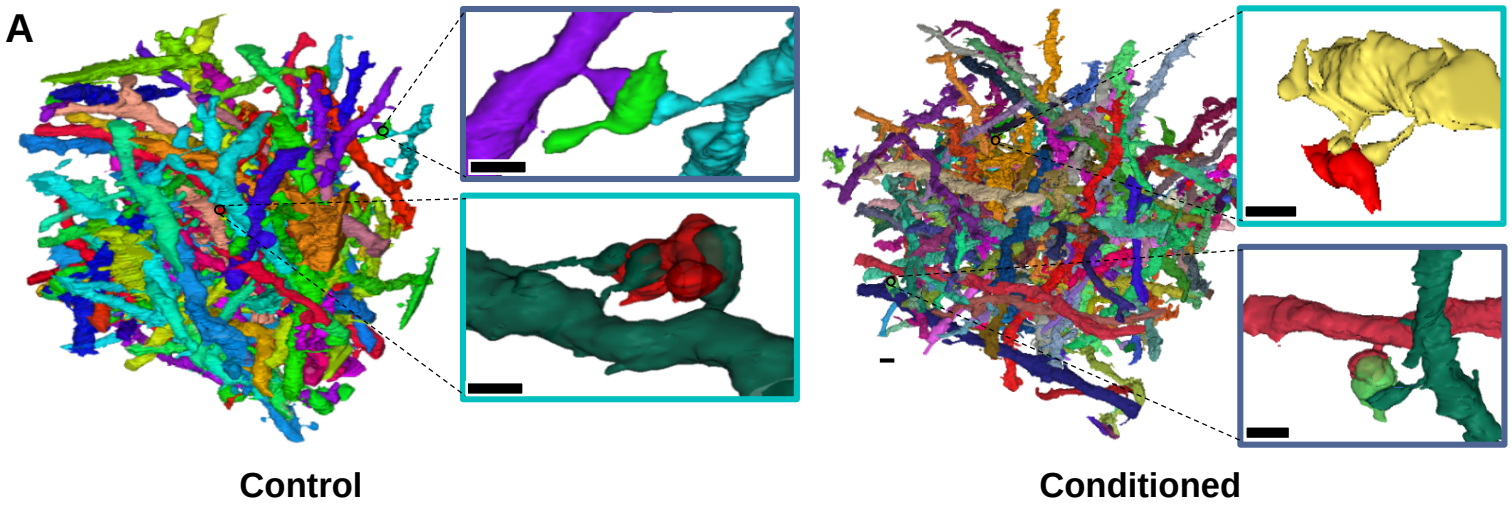

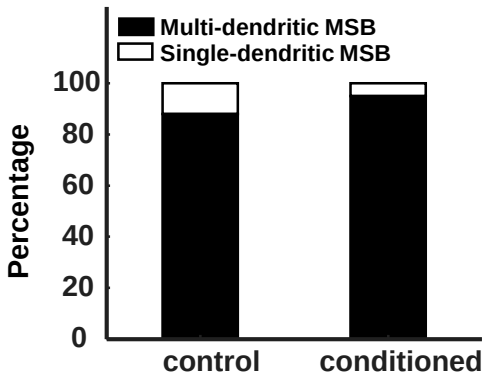

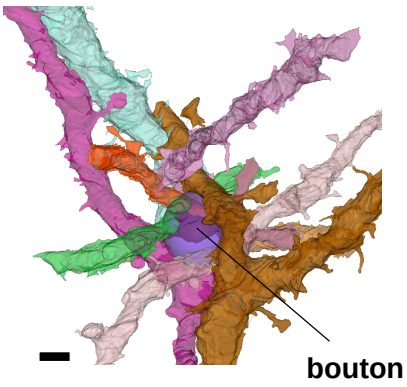

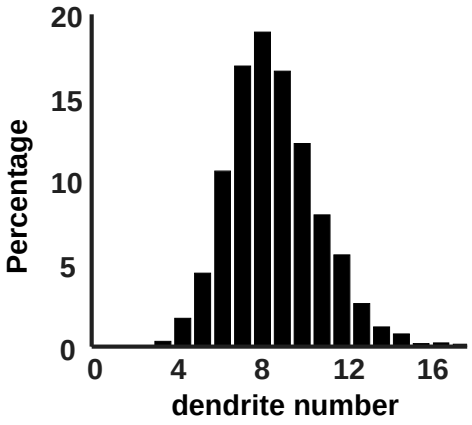

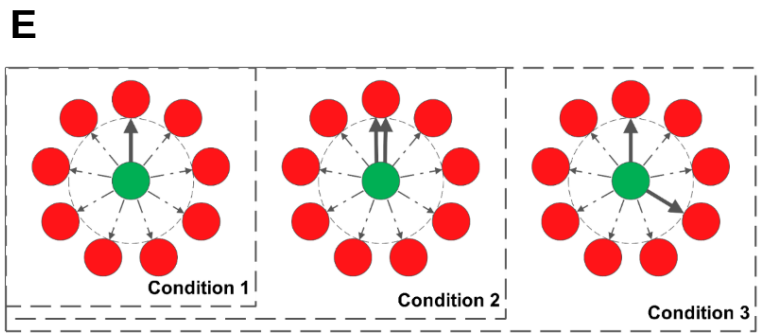

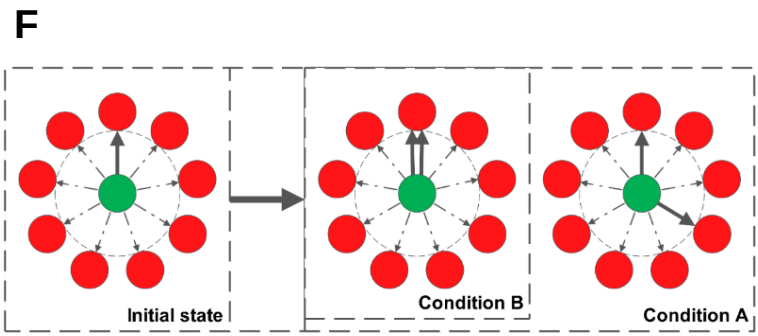

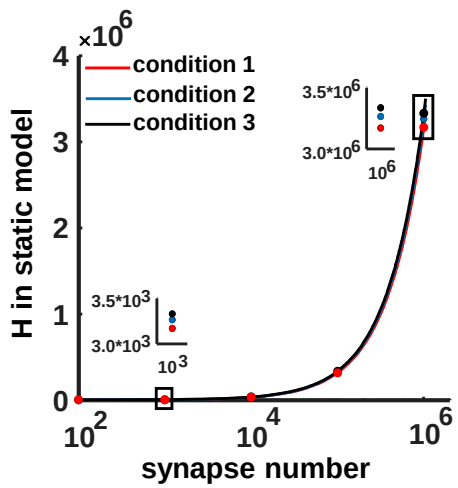

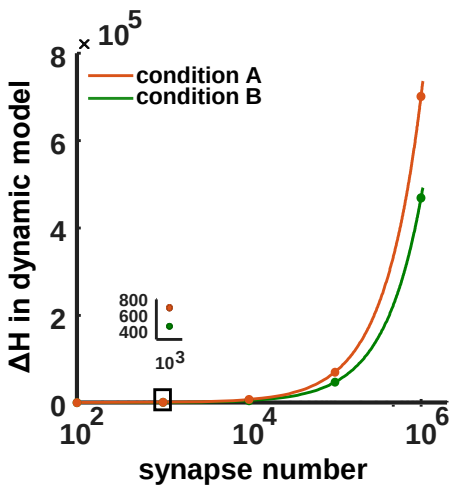

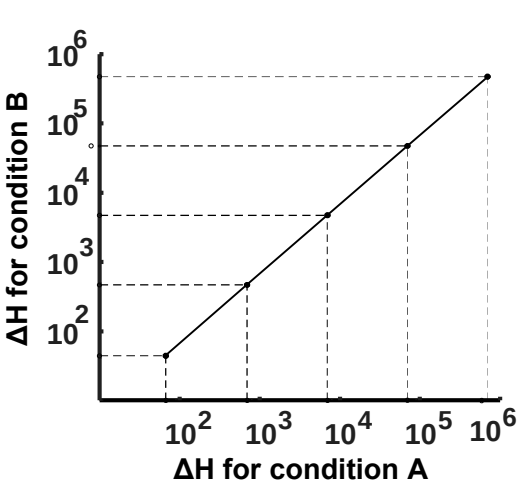

Extended Data Figure 1

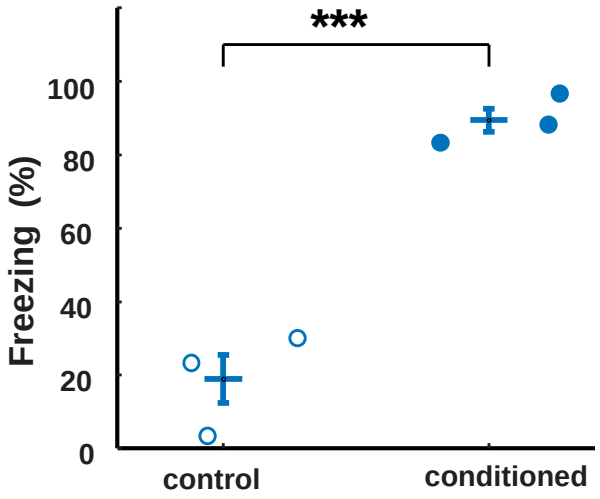

Extended Data Figure 1. Behavioral test. Behavioral results of auditory fear conditioning for control (18.89±8.01%) and conditioned (89.44±3.89%) mice. Each circle represents one mouse. $p < 0.005$, Student's t-test.

Extended Data Figure 2

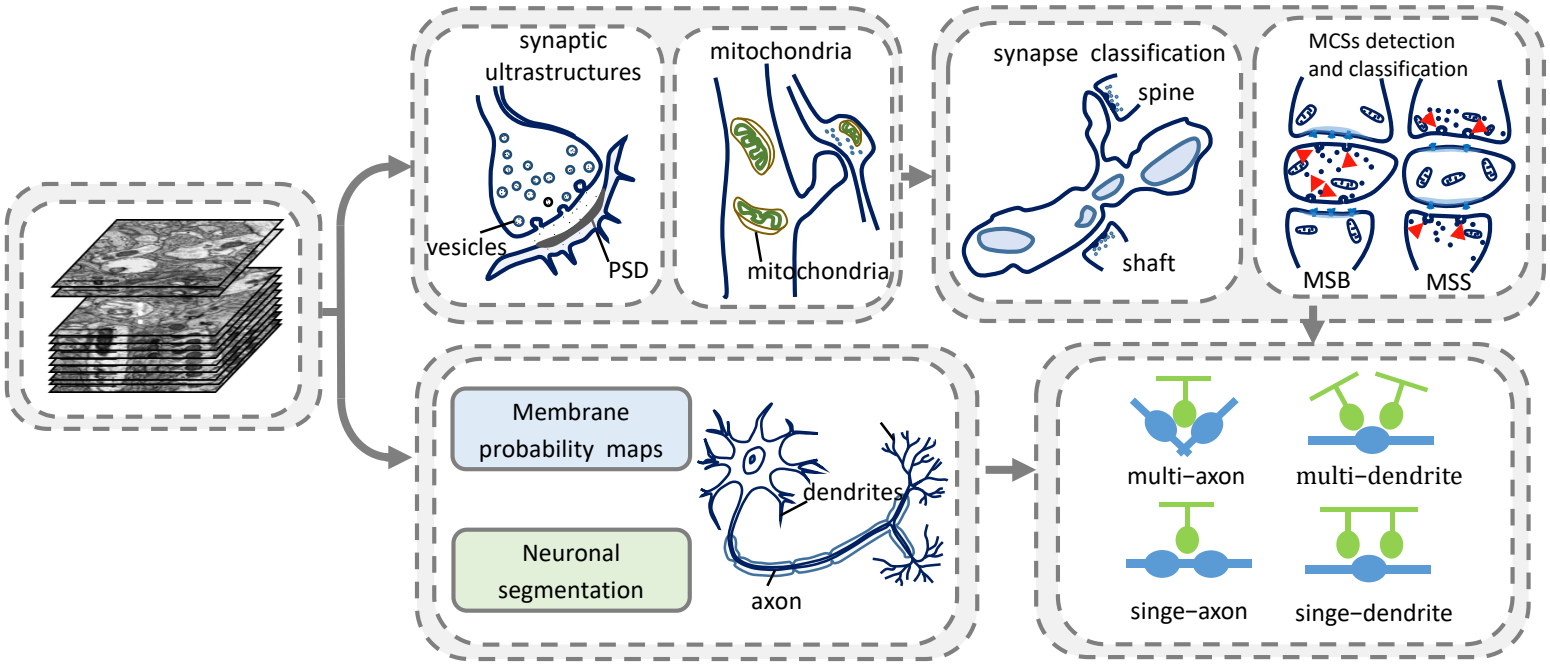

Extended Data Figure 2. Whole diagram of EM data processing procedure. The aligned EM stacks are first fed to CNNs to detect the synaptic ultrastructures (PSD and vesicle), mitochondria, and neuronal membrane. The synapses are then classified into spine or shaft synapses based on the ultrastructural features. MCSs are located and classified into two MSB or MSS. Dense segmentation is obtained by Multicut pipeline and is introduced to determine the MCSs' origination.

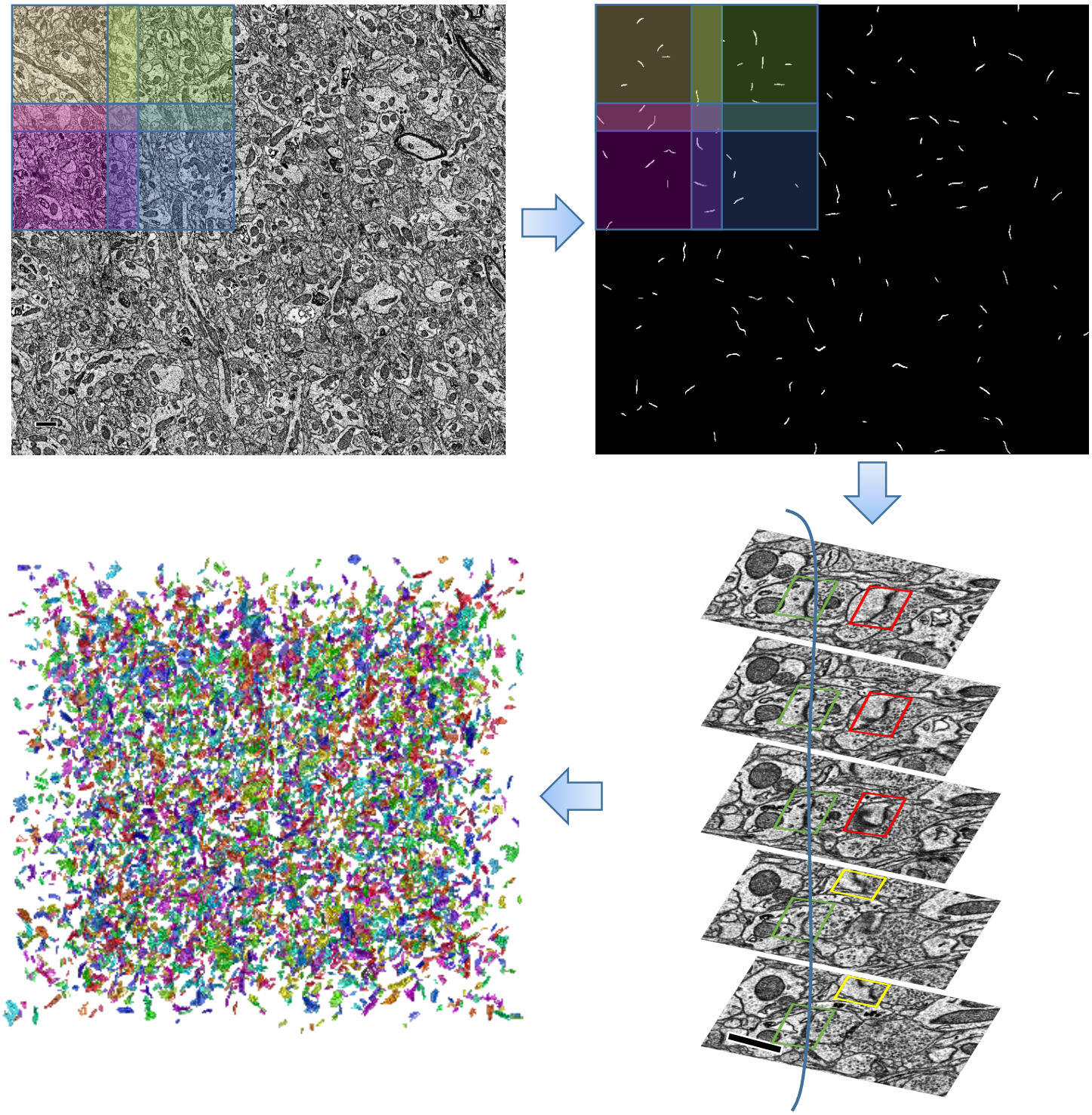

Extended Data Figure 3. Pipeline of synapses reconstruction from ssEM images. The original image are cropped into overlapping small patches. The patches are fed into the trained network for synapse inference, and the overlapping areas are fused using the single-layer fusion algorithm. The multilayer 3D connection algorithm is applied to obtain the reconstructed synapses. 3D visualization is shown in ImageJ.

Extended Data Figure 4

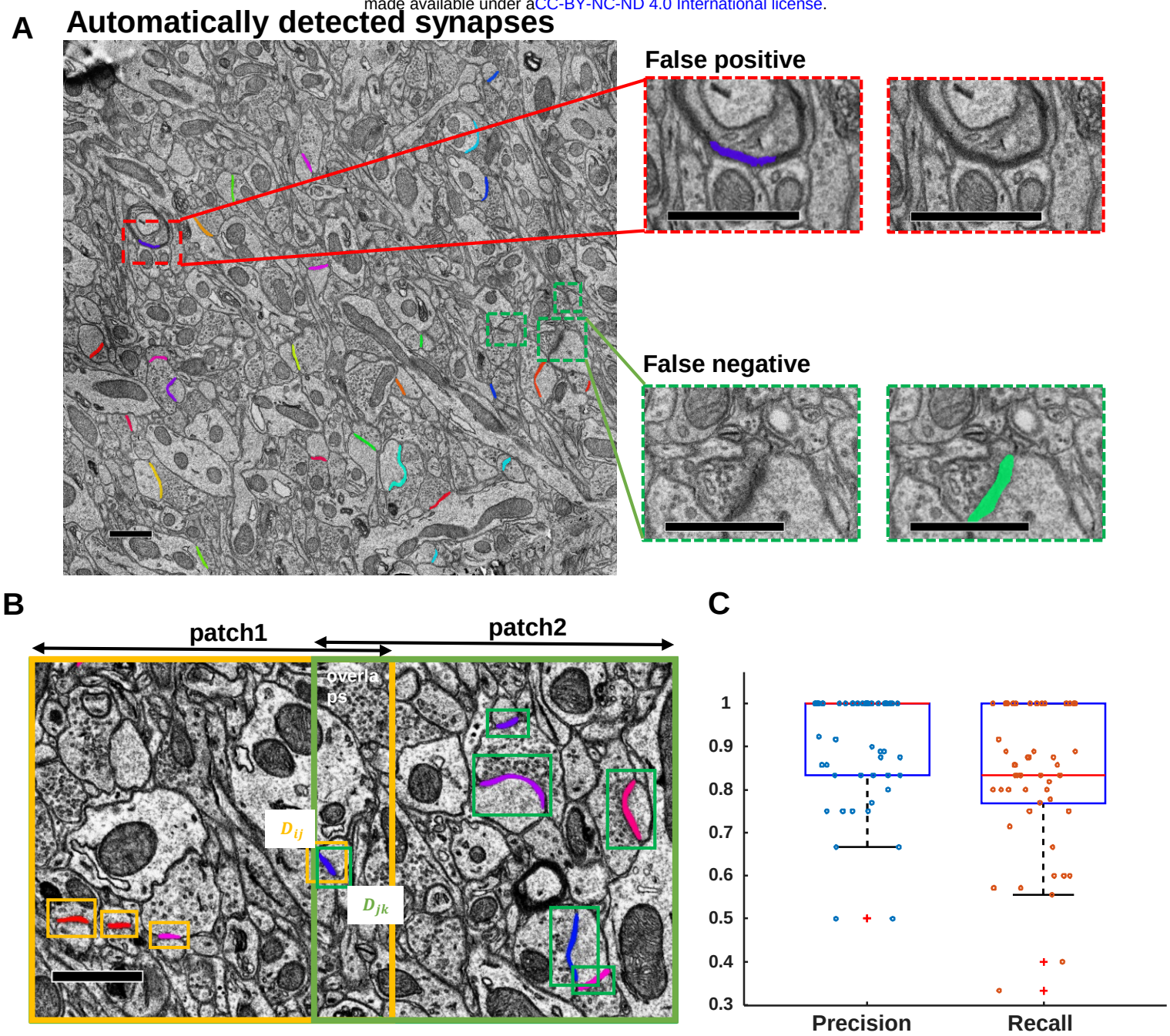

Extended Data Figure 4. Automatic detection of synapses.

(A) Examples showing automatically detected synapses in an EM image. Colored thick lines represent automatically detected synaptic clefts. Insets show false positives and false negatives identified by manual verification. Scale bar: 1μm.

(B) Diagram of single-layer fusion algorithm. Orange and green boxes represent two cropped patches with overlap. D_{ij} and D_{jk} are repeated detection boxes in overlapping region. Scale bar: 1μm.

(C) Evaluation on the synapse test set in terms of precision and recall. Each circle indicates an image from the test set.

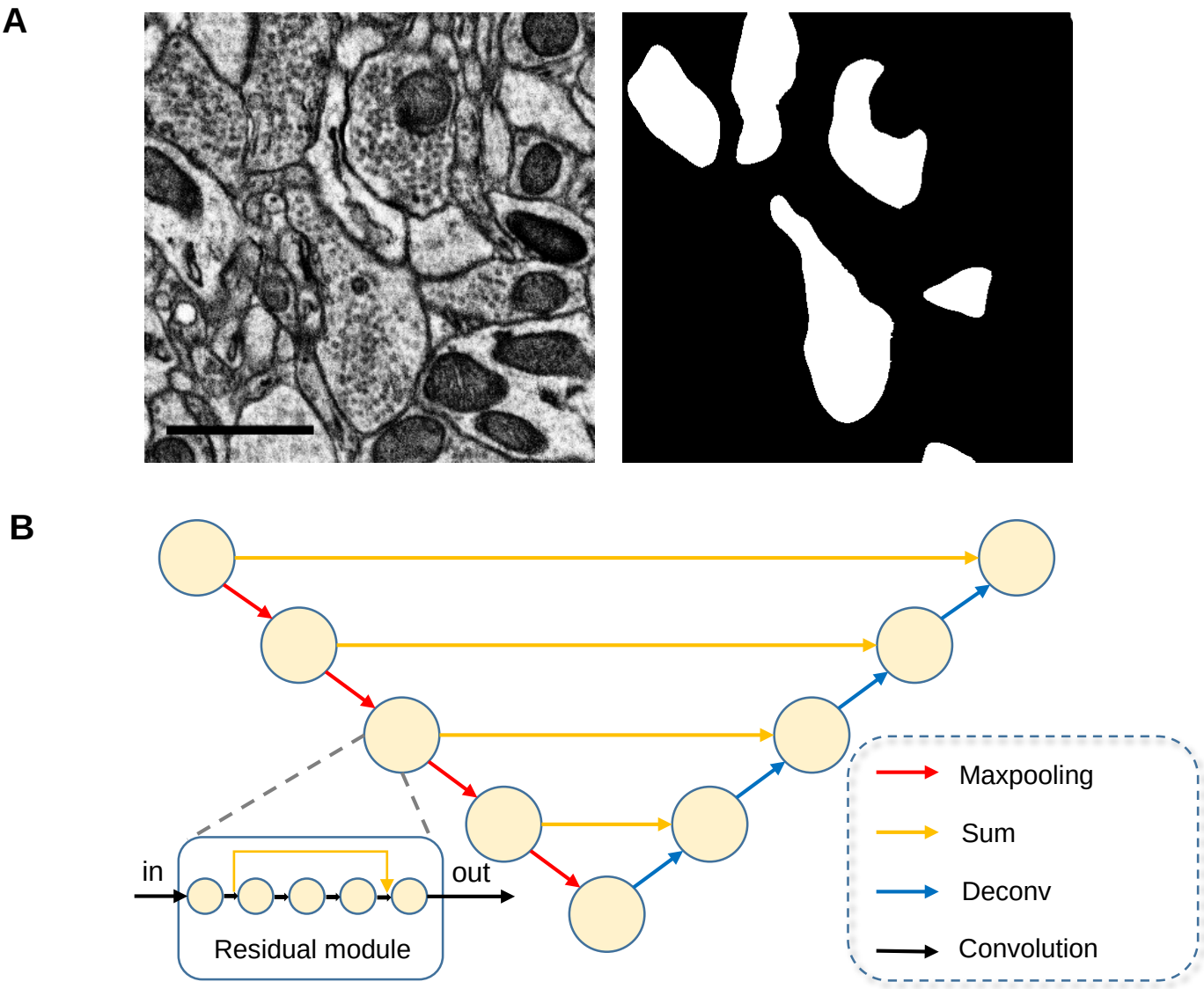

Extended Data Figure 5. Identification of vesicle clouds.

(A) Examples of EM image and binary vesicle cloud mask predicted by CNN. Scale bar: 1 μm.

(B) Network architecture of FusionNet, which takes a 1,024×1,024 image patch as input and outputs the binary vesicle cloud masks of input image. One golden circle represents a residule module. The yellow arrows indicate the sum operation to fuse features from encode path and decode path. Red arrows and blue arrows indicate the convolution with maxpooling and deconvolution operations, respectivey.

Extended Data Figure 6

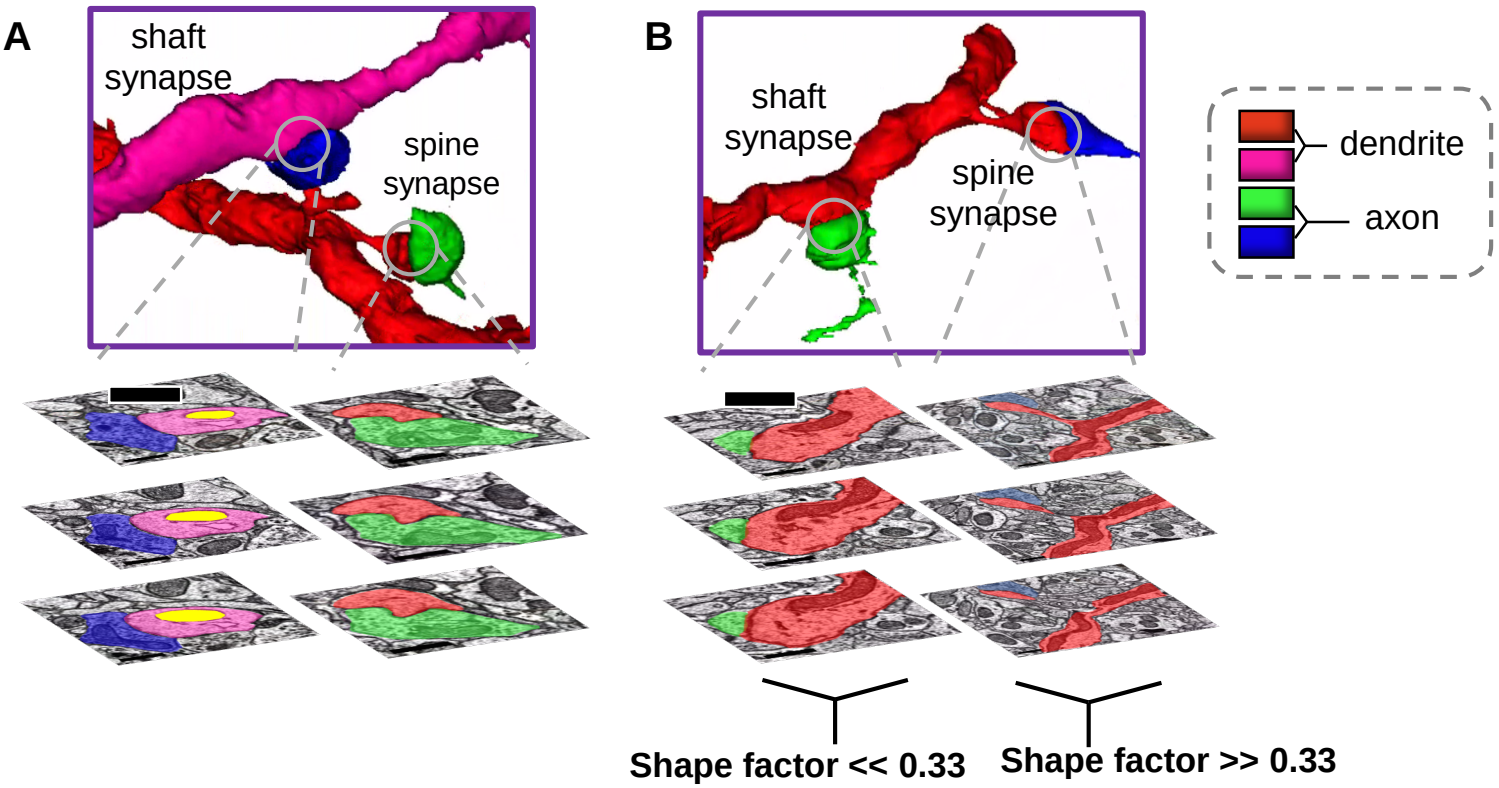

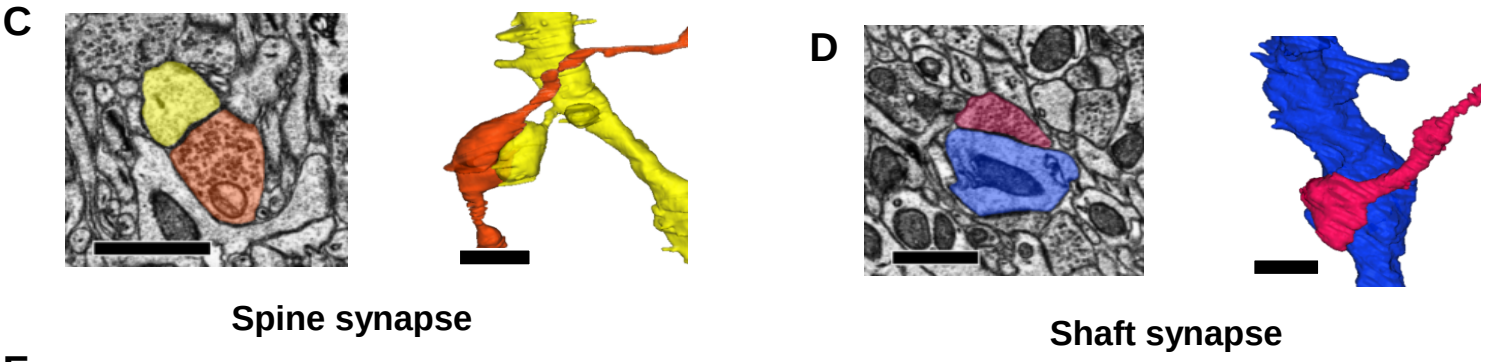

E

Predict \ Ground truth	spine	shaft
spine	445	13
shaft	12	89

Extended Data Figure 6. Classification of spine and shaft synapses.

(A) Spine and shaft synapse classification based on the lack (right) or existence (left) of mitochondria (yellow) in postsynaptic structures. Scale bar: 1 μm.

(B) Spine and shaft synapse classification based on spiny (right) or flat (left) postsynaptic structures. Scale bar: 1 μm.

(C-D) Example of 3D reconstructed spine and shaft synapse. Scale bar: 1 μm.

(E) Confusion matrix of classification results on the test dataset.

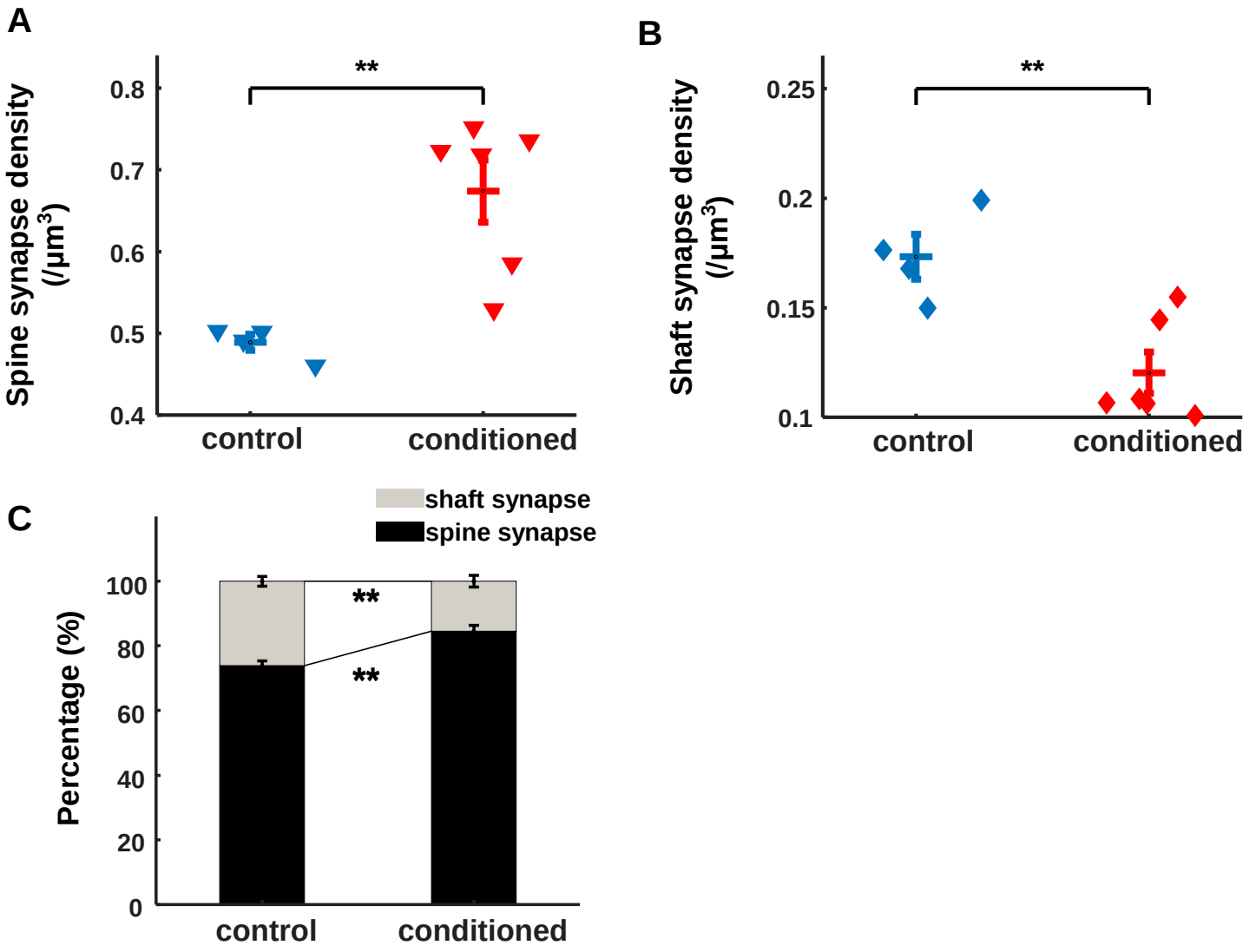

Extended Data Figure 7. Changes of spine and shaft synapses in A1 after AFC.

(A) Spine synapse density is higher in the conditioned mice ($0.674 \pm 0.0379/\mu m^3$) than in controls ($0.489 \pm 0.0099/\mu m^3$). $p<0.01$， two-sided *t*-test.

(B) Shaft synapse density is lower in the conditioned mice ($0.12 \pm 0.0094/\mu m^3$) than in controls ($0.173 \pm 0.0102/\mu m^3$). $p<0.01$， two-sided *t*-test.

(C) Shaft and spine synapse proportion in the control mice (spine: $73.84 \pm 1.49\%$, shaft: $26.16 \pm 1.49\%$) and conditioned mice (spine: $84.54 \pm 1.81\%$, shaft: $15.47 \pm 1.81\%$) . $p<0.01$， two-sided *t*-test.

Extended Data Figure 8

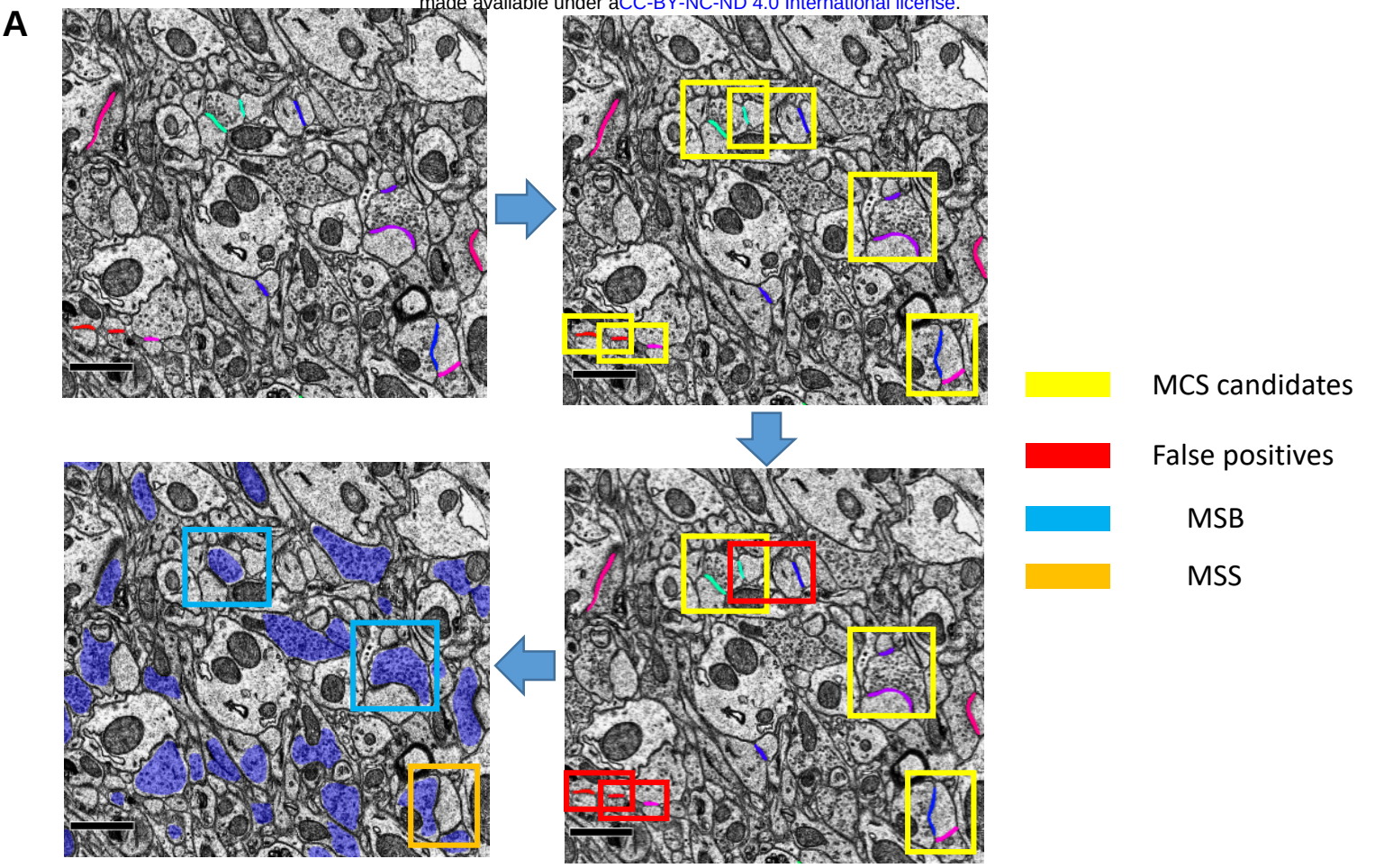

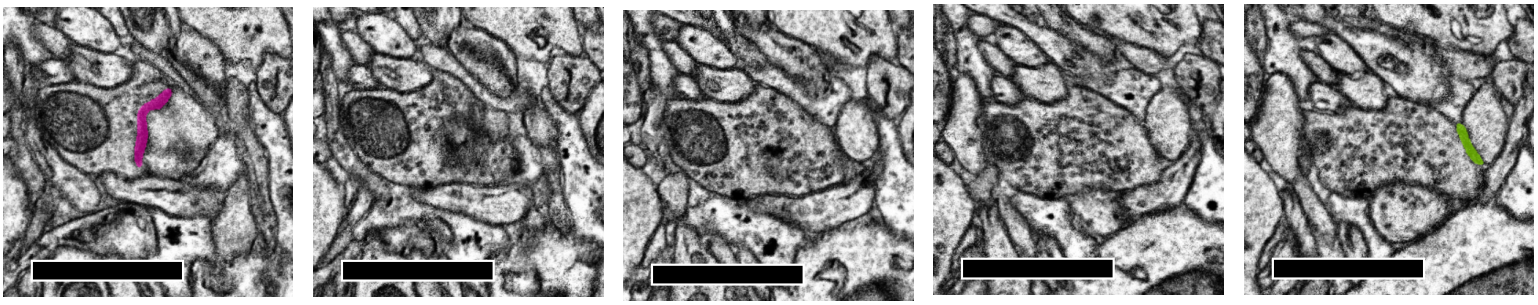

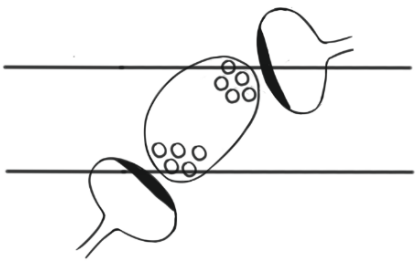

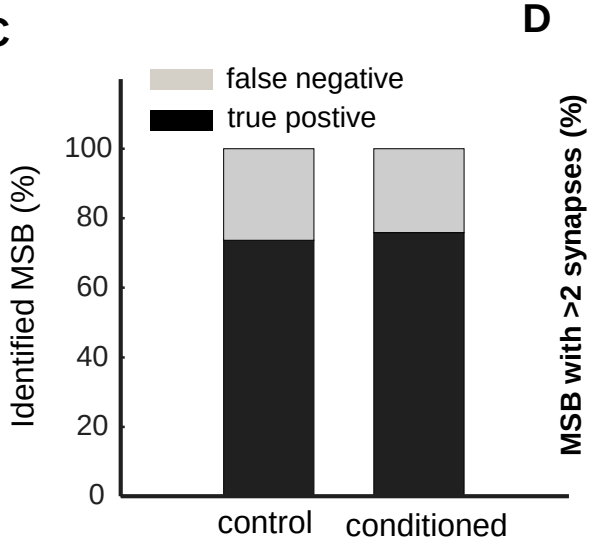

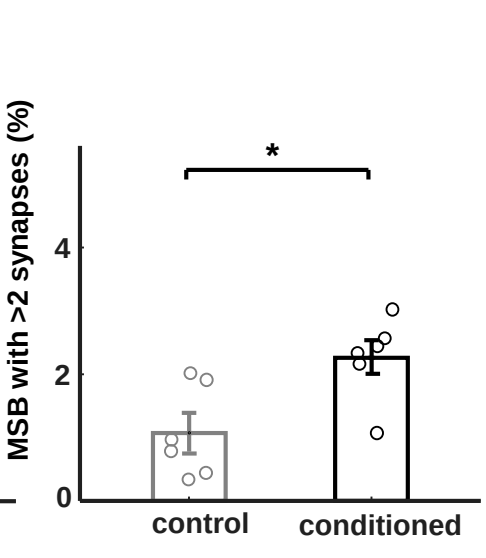

Extended Data Figure 8. Semi-automatic detection, verification and classification of MCSs.

(A) MCSs detection and verification. MCS candidates are first automatically marked based on a close-vicinity criterion, and then manually verified and classified into MSBs or MSSs based on the vesicle cloud features. Colored line: PSD; yellow box: MCS candidates; red box: false detection; blue box: verified MSB; orange box: verified MSS; blue patch: boutons. Scale bar: 1 μm.

(B) A continuous series of EM images showing an MSB that was omitted by the automatic close-vicinity detection algorithm because the two spines never co-appeared on a single slice. Bottom left: a cartoon illustrating the false negative scenario. Scale bar: 1 μm.

(C) False negative rate of MSBs estimated by manual identification of MSBs in saturated reconstruction blocks (control: 26.3%, 11 × 12 × 5 mm, conditioned: 24%, 17 × 14 × 2.5 mm).

(D) The percentage of MSB synapses having more than 2 postsynaptic sites is higher in the conditioned mice (2.26±0.3 %) than in controls (1.07±0.3%). $p < 0.05$, two-sided t-test.

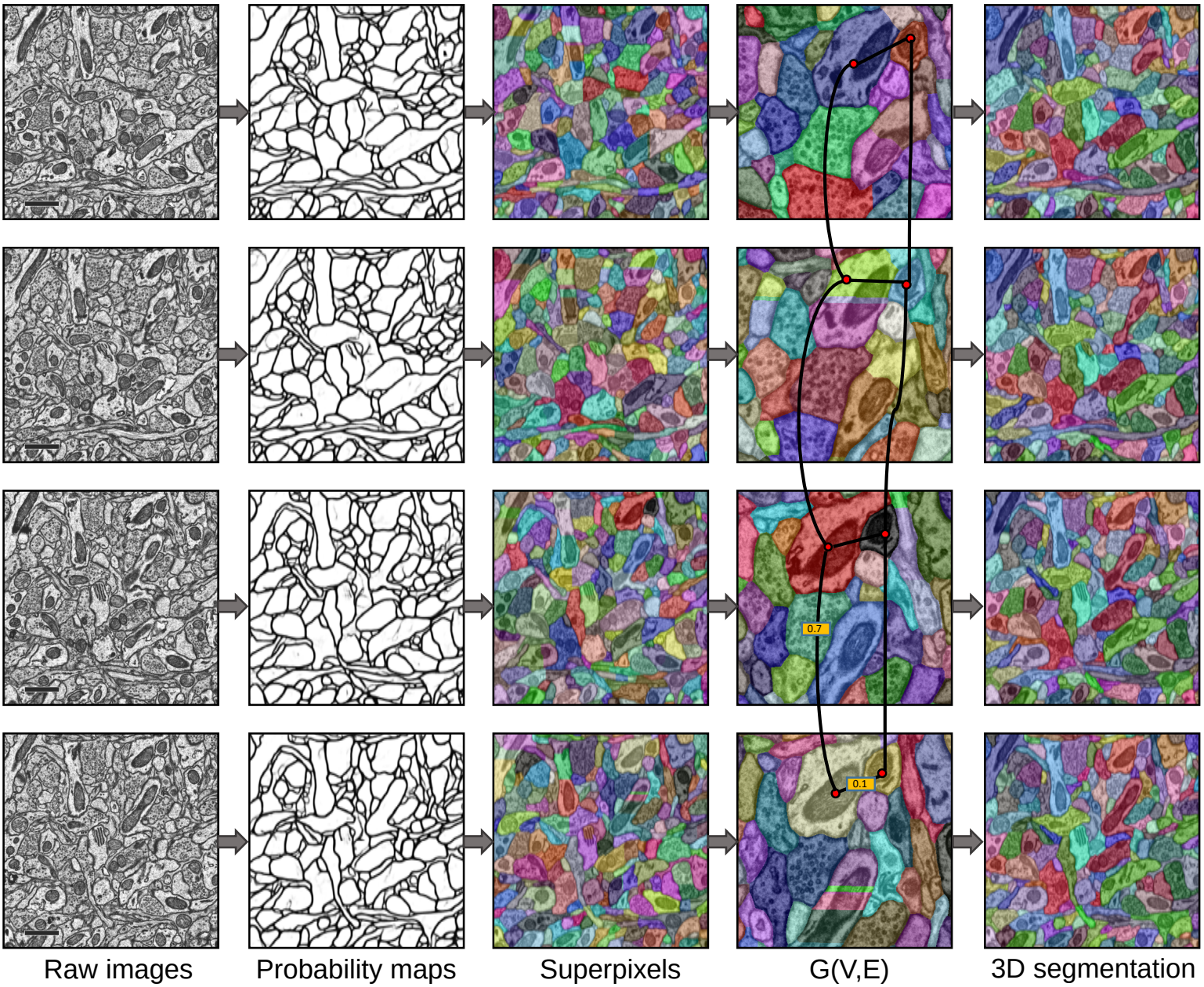

Extended Data Figure 9. Workflow of volume segmentation. Trained network takes raw images as input and membrane probability maps as output, then distance transform is applied to create superpixels and a graph G is constructed to build the relationships between segments. 3D segmentation results are obtained by solving the graph partitioning problem. Scale bar: 1 μm.

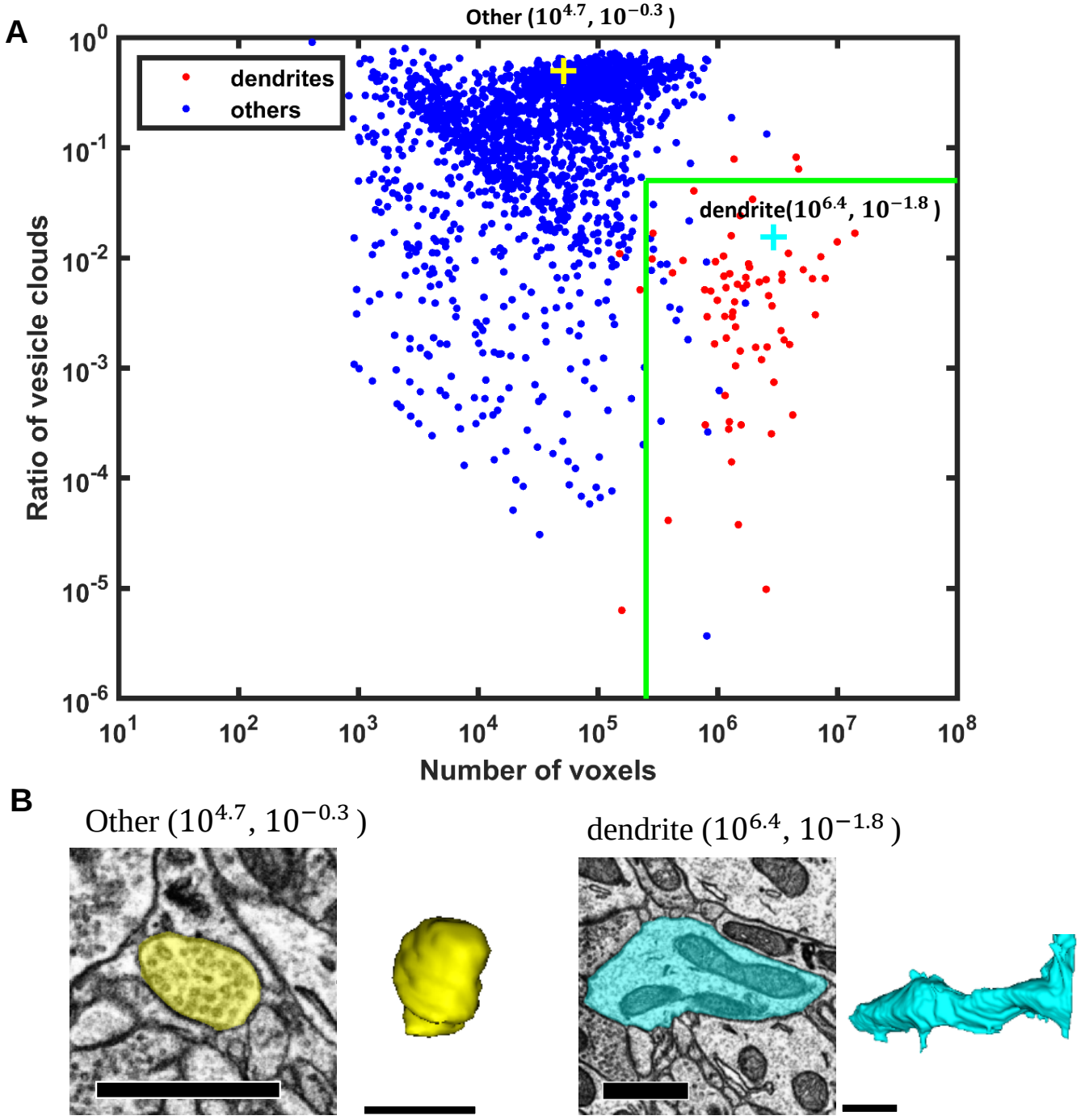

Extended Data Figure 10. Identification of dendrites from saturated reconstruction.

(A) Each point represents a dendrite or non-dendrite (other) segment.

(B) Examples of identified axonal bouton (yellow) and dendritic branch (blue). Scale bar: 1 μm.

Methods

Animals

C57BL/6 mice were purchased from SLAC Laboratory Animals (Shanghai, China). YFP-H line mice were obtained from the Jackson Laboratory (Bar Harbor, ME, USA). Mice were bred and housed in the animal facility of Shanghai Protein Center under a 12 h light-dark cycle (7 am-7 pm light). Eight- to twelve-week-old male and female mice were used for the experiments. All procedures were approved by the Animal Committee of the Shanghai Tech University.

Behavior

Fear conditioning and behavioral test for the freezing response took place in different environments. Mice were handled prior to conditioning. A commercial fear conditioning apparatus (MED Associates Inc., St. Albans, VT, USA) was used for the fear conditioning and behavioral test. Before conditioning and testing, the apparatus was wiped clean with 70% ethanol. The conditioned stimulus (CS) is a series of 14 kHz beeps (interleaved 0.5 s on, 0.5 s off) at 80 dB, lasting 10s in total; the unconditioned stimulus (US) is a 0.6 mA foot shock lasting 2 s. The sound co-terminates with the foot shock. For conditioned animals, CS-US pairing was presented 5 times with random intervals ranging from 60 to 90 s. For naïve animals, CS was presented 5 times with random intervals, without presentation of US. The behavioral responses to CS were tested 1 day after conditioning for both groups, using CS lasting 60 s. All conditioned animals showed high levels of freezing when CS was played, and naïve animals did not show a freezing response (Extended Data Figure 1).

Electron microscopy sample preparation

The mouse was deeply anaesthetized with sodium pentobarbital (50 mg/kg, i.p.) and transcardially perfused with freshly prepared 4% paraformaldehyde and 0.5% glutaraldehyde (EM grade) in phosphate-buffered saline (PBS) 3 days after behavioral training. The brain was post-fixed in 2% paraformaldehyde and 2% glutaraldehyde overnight in a cold room. Blocks of the auditory cortex were dissected and embedded in resin for serial sectioning. Serial sections of the samples were continuously sectioned at 50 nm with an ATUMtome automated tape-collecting ultramicrotome (RMC, Boeckeler instruments Inc., Tucson, AZ, USA) and then collected onto a Kapton polyimide tape (8 mm wide and 100 μm thick). The tape with brain sections were then segmented and attached to 4-inch silicon wafers *via* double coated carbon conductive tape (TED Pella Inc, Redding, CA, USA). Lastly, the wafers were coated with 6 nm of carbon though an EM ACE60 high vacuum film deposition instrument (Leica

Microsystems GmbH, Wetzlar, Germany) to prevent charging during scanning EM imaging (Figure 1).

Electron Microscopy

The tape-collected ultra-thin sections were imaged on a Carl Zeiss Supra 55 scanning electron microscope (Carl Zeiss AG,. Oberkochen, Germany) using a secondary electron detection (9 kV accelerating potential, working distance of approximately 6.0 mm), with resolution of 2-4 nm/pixel and pixel dwelling time of 1.5 μs.

Image Alignment

To correct for distortions of serial sections from automated tape-collecting ultramicrotome scanning electron microscopy (ATUM-SEM), we used a non-linear registration algorithm[38] to create 3D image stacks that retain the original morphology as much as possible. We assumed that the tissue deformations on different sections were independent. In order to extract reliable correspondences between adjacent sections, we used the dense correspondence matching SIFT-flow algorithm[39]. Then, the corresponding points on different sections were simultaneously adjusted based on an energy function to retain the same x-y coordinates. In addition, the displacements of these corresponding points were constrained to be smooth and small, thereby restricting the non-linear deformation of the original images. Finally, with the displacement vector of the extracted corresponding points, the positions of the points in the original sections, as well as in the aligned images, were obtained. The Moving-Least-Square (MLS) method[40] was used to warp each section image. The deformation result produced by the MLS method was globally smooth, and the biological tissue could retain its shape as a result of the rigid local transformation.

Network Architecture of FPN

The FPN consists of a bottom-up pathway and a top-down pathway with lateral connections. The bottom-up pathway leverages the hierarchy of the natural pyramid features of the ResNet50, and the top-down pathway recovers the original resolution by using the upsample layer step by step. On each level of the pyramid, the top-down pathway features will be fused (element-wise addition) with the bottom-up pathway features in the corresponding level. By constructing the feature pyramid, the lower-resolution feature maps contain more semantic information, while the higher-resolution feature maps contain more detailed information. The scale-space induced from the feature pyramid fits well with the object-space. Thus, the RPN and R-CNN predict the class and regress the bounding box of objects at different scale using feature maps at different levels of the pyramid. The same applies for the mask branch. Specifically, the feature pyramid has 5 levels and the corresponding object scales are 32, 64, 128, 256,

512, respectively.

Block-wise inference strategy for large-scale data

Due to the constraints of the GPU, the inference was designed to proceed in a block-wise way for large-scale data (Extended Data Figure 4B). The original images were first cropped into small patches ($2{,}048 \times 2{,}048$) with overlaps (100×100), which were then fed into the trained network to generate detection boxes and segmentation masks. To obtain the connection relationship at the 3D level, we used a strategy which first fused the results on 2D and then connected the adjacent 2D layers to produce the 3D results.

To facilitate the description of our algorithm, we defined N_i as the number of detection boxes in the i-th layer, and D_{ij} represented the j-th synaptic detection box in the i-th layer:

$$D_{ij} = (x_{ij}^1, y_{ij}^1, x_{ij}^2, y_{ij}^2)$$

where $x_{ij}^1, y_{ij}^1, x_{ij}^2, y_{ij}^2$ represented the left-upper coordinate, left-upper coordinate, right-lower coordinate and right-lower coordinate, respectively; $D_i = \{D_{ij},\ j = 1,2,\dots,N_i\}$ denoted the set of all detection boxes on the i-th layer. C_{ij} represented the corresponding segmentation result of the j-th synapse in the i-th layer. $C_i = \{C_{ij},\ j = 1,2,\dots,N_i\}$ represented the set of all binary segmentation results in the i-th layer.

（1）Single-layer fusion algorithm for detection and segmentation results

After obtaining the synaptic detection and the segmentation results of small patches by deep neural network, we stitched them to recover the original image size. At the overlapping region, there could be multiple different detection results for the same synapse. In this case, the synapse was repeatedly detected. Therefore, we designed an iterative 2D fusion algorithm to fuse the detection bounding boxes and corresponding segmentation masks in the overlapping areas. The main procedures are as follows:

Step 1: Construct the Intersection-over-Union (IoU) matrix S_i between all candidate detection boxes D_{ij} in the i-th layer. The S_i matrix can be formulated as:

$$S_i = \begin{pmatrix} s_{11}^i & s_{12}^i & \cdots & s_{1N_i}^i \\ s_{21}^i & s_{22}^i & \cdots & s_{2N_i}^i \\ \vdots & \vdots & \ddots & \vdots \\ s_{N_i1}^i & s_{N_i2}^i & \cdots & s_{N_iN_i}^i \end{pmatrix}$$

where s_{jk}^{i} represents the IoU of the j-th detection box and the k-th detection box, and the calculation formula can be expressed as follows:

$$s_{jk}^{i} = \frac{A(\cap\{D_{ij}, D_{ik}\})}{A(\cup\{D_{ij}, D_{ik}\})}, j = 1,2, \dots, N_i$$

where A is a function of calculating area. $\cap\{D_{ij}, D_{ik}\}$ and $\cup\{D_{ij}, D_{ik}\}$ represent the intersection and union of D_{ij} and D_{ik}, respectively. Obviously, $s_{jk}^{i} \epsilon [0,1]$. It is not difficult to find that S_i is a sparsely symmetric matrix with a main diagonal of 1.

Step 2: Find the coordinates of elements in S_i, which are greater than the threshold θ_1. Let Ind be a set, then:

$$Ind = \text{II}_{\{S_i > \theta_1\}}$$

where II denotes the indicator function. This operation acts on each element of S_i and returns the row and column number jk satisfying the condition.

Step 3: For $\forall jk \in Ind$, merge D_{ij} and D_{ik} into a new detection box D'_{ijk}. The coordinates of the new detection box are illustrated as follows:

$$D'_{ijk} = (\min(x_{ij}^{1}, x_{ik}^{1}), \min(y_{ij}^{1}, y_{ik}^{1}), \max(x_{ij}^{2}, x_{ik}^{2}), \max(y_{ij}^{2}, y_{ik}^{2}))$$

Step 4: Update N_i and D_i, and repeat above steps until no box need to be merged.

（2）Multilayer 3D connection algorithm

In order to obtain 3D synapses from the serial 2D segmentation results as well as screen out false positives, we develop and implement a 3D connection algorithm in the fine registered stacks according to the continuity of ssEM images and the spatial structural information of synapses. This procedure not only recovers synaptic morphology at the 3D level, but also assigns a unique label to each 3D synapse. The main steps are as follows:

Step 1: Construct the similarity matrix S^{it} between the synapses in the i-th layer and synapses in the t-th layer. S^{it} can be formulated as follows:

$$S^{it} = \begin{pmatrix} s_{11}^{it} & s_{12}^{it} & \cdots & s_{1N_i}^{it} \\ s_{21}^{it} & s_{22}^{it} & \cdots & s_{2N_i}^{it} \\ \vdots & \vdots & \ddots & \vdots \\ s_{N_i1}^{it} & s_{N_i2}^{it} & \cdots & s_{N_iN_i}^{it} \end{pmatrix}$$

where t = i+1. It should be noted that s_{pq}^{it} represents the ratio of the overlapping area between D_{ip} and D_{tq} to the minimum area of these two, and the calculation formula is:

$$s_{pq}^{it} = \frac{A(\cap \{D_{ip}, D_{tq}\})}{\min(A(D_{ip}), A(D_{tq}))}$$

Step 2: Find the coordinates of elements of S^{it}, which are greater than the threshold θ_2, *i.e.*

$$Ind1 = \text{II}_{\{S^{it} > \theta_2\}}$$

where II denotes the indicator function. This operation acts on each element of S^{it} and returns the row and column number pq satisfying the condition.

Step 3: For $\forall pq \in Ind1$, assign the same and unique label value to C_{tq} and C_{ip}. Then, the binary segmentation is converted into a label image.

Step 4: Repeat above steps for all layers and obtain a labeled stack. Look through all the labels to check the number of layers L^t for each label t. If L^t is less than the predefined threshold θ_3, then delete the corresponding segmentation C_{it} from the original results, which can be expressed as follows:

$$C_i = C_i \backslash C_{it}$$

After implementing the block-wise algorithm, we obtain the final result of each large image, where the same label value indicates the same synapse at the 3D level.

2D segmentation of neuronal processes

We extracted two volumes (2,048 x 2,048 x 50 voxels) from control and conditioned group as the training data for membrane detection and dense reconstruction. In the ground truth, voxels with the same value belong to the same neurite in 3D. Three experienced annotators labeled the dense labels with cross-validation.

FusionNet [23]was trained to predict the neuronal membrane. The training data was

extracted from the volume segmentation data set. Pixels that were labeled as background or at the edge of any adjacent neurite objects were collected as boundaries. The membrane probability maps obtained from the network were binarized with a threshold of 0.5, and morphologically dilated with a disk radius of 2 in order to dismiss the small cracks in membranes and avoid merge errors. A watershed algorithm was then used to obtain connected neuronal components.

Automated volume segmentation

The thickness of ssEM sections is a key factor for automatic reconstruction. High anisotropy brings more problems and challenges in learning the affinity between voxels along the Z-direction. The state-of-the-art approach, which learns an affinity graph by 3D CNN, did not perform well on our data set. Therefore, we used the Multicut pipeline [33] to analyze our data. We first applied a distance transform to generate superpixels in 2D slices. Subsequently, we constructed a 3D region adjacency graph to connect the superpixels in 2D slices as well as between sections. We then abstracted the graph as G(V, E), where the node set V denoted all the superpixels and the edge set E represented boundaries between adjacent superpixels. Then, a random forest classifier was trained to predict the scores (probability of whether an edge should be cut) of every edge in the graph to obtain a weighted un-directed graph (Extended Data Figure 9). We thus solved the graph partitioning problem with an approximate solution. Finally, we imported the segmentation results to the proofreading tool, and assigned the proofreading task to 6 experienced experimenters. The proofreading took about 4 weeks.

Experimental setup

All networks were implemented in Keras with Tensorflow[41] as backend. A stochastic gradient descent algorithm[42] with learning rate of 0.001 was used to optimize the networks. To avoid overfitting, we used online data augmentation, including random rotation, random flipping and adding random noise for all training data sets. All training and inference procedures were performed on servers equipped with NVIDIA Tesla K40 GPUs.

Spine and Shaft Synapse Classification

Excitatory and inhibitory synapses are classified according to some established criteria[43]. Due to the low axial resolution, indistinct synaptic vesicles and symmetry/asymmetry of PSDs can't be used to identify the classes of synapses. Although it is generally believed that excitatory synapses are mostly located on spines, some studies have indicated that excitatory synapses can also form on dendritic shafts[44], which cannot be quantified *in vivo* by counting spines using microscopy. Accordingly, based on the presence of postsynaptic mitochondria (Extended Data Figure 6A) and the

shape of postsynaptic structures (Extended Data Figure 6B), we established some rules to classify the spine and shaft synapses (Extended Data Figure 6C and 6D).

Previous studies have shown that there are very few mitochondria in dendritic spines, thus the absence of mitochondria can be used as one informative feature for spine identification. If no mitochondria are present in the postsynaptic site on any layer, the synapse is classified as a "spine synapse". If the proportion of mitochondria present on all layers is greater than 50%, the synapse is classified as a "shaft synapse". Since the sectioning orientation may lead to false negatives (*e.g.*, Extended Data Figure 6B), we added a morphological criterion, *i.e.*, whether the shape of the postsynaptic element is spiny or flat, for classification of remaining conditions. The mean change rate of postsynaptic areas from adjacent sections is defined as the shape factor—another informative feature for spine identification. A higher shape factor value (greater than 0.33) indicates a higher probability of existence of spines; a lower shape factor value indicates the presence of shafts (Extended Data Figure 6B). The evaluation on the test data set consisting of 559 synapses showed that our method yielded an accuracy rate of 0.95 (Extended Data Figure 6E).

Error analysis of MCS detection algorithm

The multiple boutons or spines in a single MCS had to appear on the same section for them to be successfully identified by our semi-automatic MCS detection algorithm (Extended Data Figure 8B). Indeed, a comparison against manually quantified MSB/MSS suggested that the our semi-automatic MCS detection algorithm had a false negative detection rate of 25% for two densely reconstructed image stacks (Extended Data Figure 8C). The data in Figure 5D and Figure 5E were adjusted accordingly.

Virus injection for *in vivo* imaging

The AAV-hSyn-EGFP and AAV-hSyn-tdTomato vectors were produced by Taitool Bioscience, Co., Ltd. (Shanghai, China). Virus injection was performed using a previously described protocol[3]. Briefly, mice were anaesthetized with sodium pentobarbital (7 mg/kg) and placed in a stereotaxic frame (RWD Life Sciences Co., Ltd., Shenzhen, China). For axonal labeling and imaging in the auditory cortex, 0.1-0.2 μl GFP or tdTomato viruses (~10^{13} virus particles per ml) were injected, using a glass micropipette with a Nanoject III micro-injector (Drummond Scientific Company, Broomall, PA, USA), into three different regions that project axons to the auditory cortex: lateral amygdala (LA, 1.0 mm from Bregma, 3.25 mm lateral from the midline, 3.55 mm vertical from the cortical surface), anterior cingulate cortex (ACC, −1.00 mm from Bregma, 0.5 mm lateral from the midline, and 1.5 mm vertical from the cortical surface), medial geniculate nucleus: (MGN, 3.2 mm from bregma, 2.0 mm lateral from the midline, and 2.8 mm vertical from the cortical surface).

Two-photon microscopy and data analysis

We performed cranial window implantation and two-photon imaging in mouse auditory cortex using previously described protocols[3]. Mice were imaged 1 day before and 3 days after fear conditioning. All images were analyzed using ImageJ (NIH, Bethesda, MD, USA). Dynamic turnover assays of boutons and spines were based on comparison of the images collected at two different time points (3 days after *vs*. 1 day before conditioning). Percentages were normalized to the initial image taken at 1 day before conditioning. Turnover of boutons was calculated by averaging the turnover rates of LA, ACC and MGN axonal boutons in the auditory cortex. For the dual-color labeled images, potential bouton-spine pairs were visually identified when a presynaptic bouton and a postsynaptic spine overlaid in the image stacks [3].

Details for Mathematical modeling to assess bouton and spine turnover patterns: competition/addition ratio

(1) Estimating bouton competition and addition ratio by MSS percentages and bouton turnover rate

According to the ssEM data (Figure 4G), there were 1.8% MSS synapses in control animals and 1.4% in conditioned animals. Based on *in vivo* microscopic analysis (Figure 5B), the bouton elimination rate was approximately 15% and the formation rate was 15%. We built a model starting with 120 synapses consisting of 118 1-to-1 synapses (98.3%) and 2 MSS synapses (1 MSS; 1.7%, approximated to 1.8%), and ending with 120 synapses, also 118 1-to-1 synapses and 2 MSS synapse (1.7%, approximated to 1.4%). Note that in this model, the spine entities remained the same, and the number of boutons eliminated and the number newly formed were both 18 (120 x 15%) since the number of spines and MSSs were both constant. Three major assumptions were made: 1) each bouton forms at most one synapse (MSB is not considered in this model); 2) each spine contains 1 or 2 synapses (for simplicity of modeling, we do not consider MSS containing 3 or more synapses); 3) the elimination/formation of synapses is represented by the elimination/formation of boutons.

To count all possible bouton turnover patterns, we considered bouton elimination before formation. There were a total of 3 types of bouton elimination, with the number of each type denoted as $a_k(k = 1,2,3)$ and the number of corresponding formation patterns satisfying the end situation denoted as $b_k(k = 1,2,3)$. The three types are as follows:

(1) All 18 bouton eliminations are from 1-to-1 synapses (118 in total), $a_1 = C_{118}^{18}$; All 18 bouton formations occur on above alone spines, $b_1 = 1$;

(2) There are 17 eliminations from 1-to-1 synapses and 1 from MSS synapses (2 in total), $a_2 = C_{118}^{17} C_2^1$; 17 bouton formations on above alone spines and then another one on one of the 119 candidate 1-to-1 synapses (118-17+1+17) to form MSS, $b_2 = C_{119}^1$; (3) There are 16 eliminations from 1-to-1 synapses and 2 eliminations from 1 MSS, $a_3 = C_{118}^{16} C_2^2$; 17 bouton formations on above alone spines and then another one on one of the 119 candidate 1-to-1 synapses (118-16+17) to form MSS, $b_3 = C_{119}^1$.

Thus, the total number of synaptic turnover patterns, denoted by N, can be calculated by:

$$N = \sum_{i=1}^{3} a_i b_i ,$$

Then, we calculate the formation ratio of (A.), (B.), (D.), (E.), (F.) *vs*. (C.), indicating the percentage of bouton competition and addition in new synapses, respectively. Assuming that the possibility of each synaptic turnover pattern is equal, the mathematical expectation for the number of synapses corresponding to Situation (C.) in 18 new synapses, n_{add}, and the corresponding number of new synapses where bouton competition occurs, $n_{compete}$, can be derived using the following equations:

$$n_{add} = \frac{\sum_{j=0}^{18} j N_j}{N'} ,$$

$$n_{compete} + n_{add} = 18 ,$$

where, $N_j (j = 0,1,2,\dots,18)$ is the number of synaptic turnover patterns in which only j out of 18 new synapses belong to Situation (C.). As the number of MSS after learning is only one, there can be no more than 1 addition. So $N_2 = N_3 = \cdots = N_{17} = N_{18} = 0$. $N_j (j = 0,1)$ can be obtained as follows:

$$N_0 = N - \sum_{j=1}^{18} N_j ,$$

$$N_1 = a_2 C_{101}^1 + a_3 C_{102}^1 .$$

In order to gain a better understanding of the above formula, both items in N_1 are elaborated as follows. For elimination type (2), after adding one synapse to each of the 17 alone spines, the last formed synapse to be determined is randomly added to one of 101 1-to-1 synapses that have previously remained unchanged (118-17), so the number of patterns is calculated as $a_2 C_{101}^1$. For elimination type (3), the last formed synapse to be determined is randomly added to one of 102 1-to-1 synapses that have previously remained unchanged (118-16), and thus the number of patterns is obtained as $a_3 C_{102}^1$.

Using the above equations, we determined that of the 18 new boutons, on average, 17.17 were accompanied by old bouton elimination (*i.e.*, competition) and the other 0.83 were added to existing 1-to-1 synapses to form MSSs, accounting for 95.4 and 4.6%, respectively.

In addition, we extended the model programmatically to any size regarding the number of synapses. The input parameters of the program included only the ratio of multiple-contact synapses before and after learning, turnover rate, and the number of synapses. To test our model with different parameters: the last parameter is scaled up to 12,000 and the other parameters are fixed. In general, the obtained results with different model sizes were similar, as shown in Figure 5G and Table 1.

Table 1. the bouton competition and addition ratio with different model sizes

Model size	120	1,200	12,000
$n_{compete}$ (%)	95.4%	96.3%	96.1%
n_{add} (%)	4.6%	3.7%	3.9%

(2) Estimating spine competition and addition ratio by MSB percentages and spine turnover rate

According to the ssEM data (Figure 4F), 5.0 and 6.8% of all synapses were MSB synapses in control and conditioned animals, respectively. Based on *in vivo* imaging data (Figure 5B), spine turnover rate was approximately 10% for elimination and 10% for formation. The starting 120 synapses consisted of 114 1-to-1 synapses (95%) and 6 MSB synapses (3 MSBs; 5.0%), and the end situation consisted of 121 synapses including 12 new synapses (113 1-to-1 synapses and 8 MSB synapses, *i.e.*, 4 MSBs, 6.6%, approximated to 6.8%). It should be noted that in this model, the bouton entities remain the same, and the difference between the number of synapses eliminated (11) and the number newly formed (120 x 10% = 12) is due to the constant number of boutons and variable number of MSBs. Three major assumptions were made: 1) each spine forms at most one synapse (MSS is not considered in this model); 2) each bouton contains 1 or 2 synapses; 3) the elimination/formation of synapses is represented by the elimination/formation of spines.

To count all possible spine turnover patterns, we considered spine elimination before formation. There were a total of 10 types of spine elimination, with the number of each type denoted as $a_k{}'(k = 1,2,\dots,10)$ and the number of corresponding formation patterns satisfying the end situation denoted as $b_k{}'(k = 1,2,\dots,10)$. The 10 types are as follows:

(1') All 11 spine eliminations are from 1-to-1 synapses (114 in total), $a_1{}' = C_{114}^{11}$; 11 out of 12 spine formations occur on above alone boutons and then another one on one of the 114 candidate 1-to-1 synapses (114-11+11) to form MSB, $b_1{}' = C_{114}^{1}$;
(2') There are 10 eliminations from 1-to-1 synapses and 1 from MSB synapses (6 in total), $a_2{}' = C_{114}^{10}C_3^1C_2^1$; 10 spine formations on above alone boutons and then another

two on 115 1-to-1 synapses (114-10+1+10), $b_2' = C_{115}^2$;
(3') There are 9 eliminations from 1-to-1 synapses and 2 eliminations from one single MSB, $a_3' = C_{114}^9 C_3^1 C_2^2$; 10 spine formations on above alone boutons and then another two on 115 1-to-1 synapses (114-9+10), $b_3' = C_{115}^2$;
(4') 9 eliminations from 1-to-1 synapses and 2 eliminations from two different MSBs, $a_4' = C_{114}^9 C_3^2 (C_2^1)^2$; 9 spine formations on above alone boutons and then another three on 116 1-to-1 synapses (114-9+2+9), $b_4' = C_{116}^3$;
(5') There are 8 eliminations from 1-to-1 synapses and 3 eliminations from MSBs, of which 2 are on the same MSB, $a_5' = C_{114}^8 C_3^1 C_2^2 C_2^1 C_2^1$; 9 spine formations on above alone boutons and then another three on 116 1-to-1 synapses (114-8+1+9), $b_5' = C_{116}^3$;
(6') There are 8 eliminations from 1-to-1 synapses and 3 eliminations from different MSBs, $a_6' = C_{114}^8 C_3^3 (C_2^1)^3$; 8 spine formations on above alone boutons and then another four on 117 1-to-1 synapses (114-8+3+8), $b_6' = C_{117}^4$;
(7') There are 7 eliminations from 1-to-1 synapses and 4 eliminations from 2 MSBs, $a_7' = C_{114}^7 C_3^2 (C_2^2)^2$; 9 spine formations on above alone boutons and then another three on 116 1-to-1 synapses (114-7+9), $b_7' = C_{116}^3$;
(8') There are 7 eliminations from 1-to-1 synapses and 4 eliminations from 3 MSBs, $a_8' = C_{114}^7 C_3^1 C_2^2 C_2^2 (C_2^1)^2$; 8 spine formations on above alone boutons and then another four on 117 1-to-1 synapses (114-7+2+8), $b_8' = C_{117}^4$;
(9') There are 6 eliminations from 1-to-1 synapses and 5 eliminations from 3 MSBs, $a_9' = C_{114}^6 C_3^2 (C_2^2)^2 C_2^1$; 8 spine formations on above alone boutons and then another four on 117 1-to-1 synapses (114-6+1+8), $b_9' = C_{117}^4$;
(10') There are 5 eliminations from 1-to-1 synapses and 6 eliminations from 3 MSBs, $a_{10}' = C_{114}^5 C_3^3 (C_2^2)^3$; 8 spine formations on above alone boutons and then another four on 117 1-to-1 synapses (114-5+8), $b_{10}' = C_{117}^4$.

Therefore, the total number of synaptic turnover patterns, denoted by N', can be calculated by:

$$N' = \sum_{i=1}^{10} a_i' b_i' ,$$

Then, we calculate the formation ratio of (A.), (B.), (D.), (E.), (F.) *vs.* (C.), indicating the percentage of spine competition and addition in new synapses, respectively. Assuming that the possibility of each synaptic turnover pattern is equal, the mathematical expectation for the number of synapses corresponding to Situation (C.) in 12 new synapses, n_{add}', and the corresponding number of new synapses where spine competition occurs, $n_{compete}'$, can be derived from the following equations:

$$n_{add}' = \frac{\sum_{j=0}^{12} j N_j'}{N'} ,$$

$$n_{compete}' + n_{add}' = 12 ,$$

where, $N_j'(j = 0,1,2,\dots,12)$ is the number of synaptic turnover patterns in which only j out of 12 new synapses belong to Situation (C.). As the number of MSBs after learning is 4, there can be no more than 4 additions. So, $N_5' = N_6' = \cdots = N_{11}' = N_{12}' = 0$. $N_j'\ (j = 0,1,\dots,4)$ can be obtained as follows:

$$N_0' = N' - \sum_{j=1}^{12} N_j' ,$$

$$N_1' = a_1'C_{103}^1 + a_2'C_{104}^1C_{11}^1 + a_3'C_{105}^1C_{10}^1 + a_4'C_{105}^1C_{11}^2 + a_5'C_{106}^1C_{10}^2 + a_6'C_{106}^1C_{11}^3 + a_7'C_{107}^1C_9^2 + a_8'C_{107}^1C_{10}^3 + a_9'C_{108}^1C_9^3 + a_{10}'C_{109}^1C_8^3 ,$$

$$N_2' = a_2'C_{104}^2 + a_3'C_{105}^2 + a_4'C_{105}^2C_{11}^1 + a_5'C_{106}^2C_{10}^1 + a_6'C_{106}^2C_{11}^2 + a_7'C_{107}^2C_9^1 + a_8'C_{107}^2C_{10}^2 + a_9'C_{108}^2C_9^2 + a_{10}'C_{109}^2C_8^2 ,$$

$$N_3' = a_4'C_{105}^3 + a_5'C_{106}^3 + a_6'C_{106}^3C_{11}^1 + a_7'C_{107}^3 + a_8'C_{107}^3C_{10}^1 + a_9'C_{108}^3C_9^1 + a_{10}'C_{109}^3C_8^1 ,$$

$$N_4' = a_6'C_{106}^4 + a_8'C_{107}^4 + a_9'C_{108}^4 + a_{10}'C_{109}^4 .$$

The first three items in N_1' are selected for detailed explanation. For elimination type (1'), after adding one synapse to each of the 11 alone boutons, the last formed synapse to be determined is randomly added to one of 103 1-to-1 synapses that have previously remained unchanged (114-11), and therefore the number of patterns is obtained as $a_1'C_{103}^1$. For elimination type (2'), the last two newly formed synapses to be determined are randomly added to one of 104 1-to-1 synapses that have previously remained unchanged (114-10) and one of other 11 "new" 1-to-1 synapses (10 1-to-1 synapses formed by 1 elimination of old 1-to-1 synapses and subsequent 1 addition; 1 1-to-1 synapse by eliminating 1 synapse of MSB), respectively. So, the number of patterns is calculated as $a_2'C_{104}^1C_{11}^1$. For elimination type (3'), the last two new synapses to be determined are randomly added to one of 105 1-to-1 synapses that have previously remained unchanged (114-9) and one of other 10 "new" 1-to-1 synapses (9 formed by 1 elimination of old 1-to-1 synapses and subsequent 1 addition; 1 formed by 2 synaptic elimination of an old MSB and subsequent 1 addition), respectively. So, the number of patterns is obtained as $a_3'C_{105}^1C_{10}^1$.

Using the above equations, we determined that of the 12 new spines, on average, 8.78 were accompanied by old spine elimination (i.e., competition) and the other 3.22 were added to existing 1-to-1 synapses to form MSBs, accounting for 73.2 and 26.8%, respectively.

In addition, we also developed the model programmatically for any model size about the number of synapses. In general, the obtained results with different model sizes are similar, as shown in Figure 5H and Table 2.

Table 2. the spine competition and addition ratio with different model sizes

Model size	120	1,200	12,000

$n_{compete}$ (%)	73.2%	72.6%	72.8%
n_{add} (%)	26.8%	27.4%	27.2%

Calculating the number of dendrites intersecting within 1-μm radius of a bouton

Based on the dense reconstruction results, we formulated some criteria to identify each neurite as dendritic or not. We extracted a 2D vector (number of voxels and ratio of vesicle cloud) as features to classify the segments. If the number of voxels in a neurite was greater than 250,000 and the ratio of vesicle cloud in it was less than 5%, this neurite was classified as dendritic (Extended Data Figure 10). For each bouton, we fit a minimum circumscribed circle and obtained the radius (R) and center (x, y, z) approximately. Then, we extended a sphere centered on (x, y, z) with radius of R+1 μm, and the number of dendrites that pass through the sphere was calculated.

Details for Static Connectivity Model

For simplicity, our model consists of 100 synaptic connections (Figure 6E). Based on our experimental data (Figure 6D), each bouton can make contact with its 9 potential dendrites. There are two notable constraints: 1) at most 2 synapses can be formed per bouton; 2) 6% of the synapses are MSB synapses (Figure 5G) for conditions 2 and 3.

For condition 1, the constraint of the number of synapses and only one synapse formed per bouton makes the existence of exactly 100 boutons. Each independent bouton has C_9^1 possible connections, so there is a total of $(C_9^1)^{100}$ patterns for condition 1.

For condition 2, since 6% of synapses are MSB synapses, there are a total of 6 MSB synapses from 3 MSBs. Thus, this condition consists of 97 boutons including 94 1-to-1 boutons and 3 MSBs. Accordingly, the number of patterns for condition 2 can be given by $C_{97}^3(C_9^1)^{94}(C_9^1)^3$. In other words, the selection of 3 MSBs from 97 boutons and the independent connection of each bouton are all factors that contribute to the increase of the number of patterns.

For condition 3, each of the 3 boutons selected as MSBs has $(C_9^2 + C_9^1)$ optional connection patterns that meet the condition. Rethinking the consideration of condition 2, the total number of patterns that meet condition 3 can be calculated as $C_{97}^3(C_9^1)^{94}(C_9^2 + C_9^1)^3$.

In detail, we express the respective calculation equations of information entropy that satisfy conditions 1, 2 and 3, as follows:

$$H_{condition1} = -\sum_{i=1}^{(C_9^1)^{100}} \frac{1}{(C_9^1)^{100}} log_2 \frac{1}{(C_9^1)^{100}} = 317bits\,,$$

$$H_{condition2} = -\sum_{i=1}^{C_{97}^3 (C_9^1)^{97}} \frac{1}{C_{97}^3 (C_9^1)^{97}} log_2 \frac{1}{C_{97}^3 (C_9^1)^{97}} = 325bits\,,$$

$$H_{condition3} = -\sum_{i=1}^{C_{97}^3 (C_9^1)^{94} (C_9^2 + C_9^1)^3} \frac{1}{C_{97}^3 (C_9^1)^{94} (C_9^2 + C_9^1)^3} log_2 \frac{1}{C_{97}^3 (C_9^1)^{94} (C_9^2 + C_9^1)^3} = 332\ bits\,,$$

where, C_n^m is the combinatorial number with respect to n and m.

Thus, including an MSB that connect to the same dendrite increases the ISC by 2.5% in this model, and the connectivity of the MSB to multiple dendrites increases another 2.2%. The results hold when we scale up the model tenfold each time up to 10^6 synapses (Figure 6G). The information entropy values of 3 conditions under 5 model scales are listed in Table 3. The benefits of adding MSBs remained when the model was scaled up to 10^6 synapses (Figure 6G).

Table 3. The information storage capacity (ISC) of a static neural network

Model scale	10^2	10^3	10^4	10^5	10^6
Condition 1	317 bits	3,170 bits	31,699 bits	316,993 bits	3,169,925 bits
Condition 2	325 bits	3,264 bits	32,673 bits	326,781 bits	3,267,872 bits
Condition 3	332 bits	3,334 bits	33,370 bits	333,747 bits	3,337,529 bits

Details for Dynamic Connectivity Model

We built a neural network model that incorporated plasticity by adding 10% more contacts to the boutons as a form of learning-induced synaptic formation. Plasticity is represented by a 10% increase in synaptic connections by adding 10 connections to existing boutons in a network consisting of 100 boutons and 100 1-to-1 synapses. There are two notable constraints: 1, at most one synapse is added to each bouton; 2, formation of the new synapses is random.

Before the synaptic formation, the number of possible connections for both conditions A and B was $(C_9^1)^{100}$, which is the same as condition 1 of the static model.

For condition B, new connections can only be formed on the same dendrite. Therefore, only the factor of the selection of the 10 boutons from the 100 boutons to form new synapses can lead to an increase in the number of patterns triggered by the synaptic formation. Furthermore, the number of patterns after formation can be written as $C_{100}^{10}(C_9^1)^{90}(C_9^1)^{10}$.

For condition A, like condition 3 in the static model, each of the 10 boutons selected as MSBs has $(C_9^2 + C_9^1)$ optional connection patterns that meet the criterion. Rethinking the consideration of condition B, the total number of patterns that meet condition A can be calculated as $C_{100}^{10}(C_9^1)^{90}(C_9^2 + C_9^1)^{10}$. We can obtain the increase of information entropy for conditions A and B, as follows:

$$\Delta H_{conditionA} = -\sum_{i=1}^{C_{100}^{10}(C_9^1)^{90}(C_9^2+C_9^1)^{10}} \frac{1}{C_{100}^{10}(C_9^1)^{90}(C_9^2+C_9^1)^{10}} log_2 \frac{1}{C_{100}^{10}(C_9^1)^{90}(C_9^2+C_9^1)^{10}}$$

$$-\left(-\sum_{i=1}^{(C_9^1)^{100}} \frac{1}{(C_9^1)^{100}} log_2 \frac{1}{(C_9^1)^{100}}\right) = 67\ bits\,,$$

$$\Delta H_{conditionB} = -\sum_{i=1}^{C_{100}^{10}(C_9^1)^{100}} \frac{1}{C_{100}^{10}(C_9^1)^{100}} log_2 \frac{1}{C_{100}^{10}(C_9^1)^{100}} - \left(-\sum_{i=1}^{(C_9^1)^{100}} \frac{1}{(C_9^1)^{100}} log_2 \frac{1}{(C_9^1)^{100}}\right)$$

$$= 44\ bits\,.$$

Clearly, in a plastic network, the possibility of a bouton connecting to multiple dendrites dramatically increases the information entropy added by synaptic plasticity. The results hold when we scale up the model tenfold each time up to 10^6 synapses (Figure 6H). The increase of information entropy values of 2 conditions under 5 model scales is shown in Table 4. Notably, whereas multi-dendritic MSB only slightly adds to the ISC in a static network (Figure 6G), the increase in the ISC for condition A by adding synapses is more than 50% (Figure 6H) higher than that of condition B in the plastic network. The relative advantage of multidendritic connectivity in ΔH scaled linearly with the network size (Figure 6I).

Table 4. the increase of the ISC of a dynamic neural network

Model scale	10^2	10^3	10^4	10^5	10^6
Condition A	67 bits	697 bits	7,006 bits	70,111 bits	701,179 bits

Condition B	44 bits	464 bits	4,684 bits	46,892 bits	468,986 bits